

# Characteristics of ocean mesoscale eddies in the Canadian Basin from a high resolution pan-Arctic model

Noémie Planat<sup>1</sup>, Carolina O. Dufour<sup>1,2</sup>, Camille Lique<sup>2</sup>, Jan K. Rieck<sup>1</sup>, Claude Talandier<sup>2</sup>, and L. Bruno Tremblay<sup>1</sup>

<sup>1</sup>McGill University, Departement of Atmospheric and Oceanic Sciences, Montréal, Québec, Canada

<sup>2</sup>University of Brest, CNRS, Ifremer, IRD, Laboratoire d'Océanographie Physique et Spatiale (LOPS), IUEM, F29280, Plouzané, France

**Correspondence:** Noémie Planat (noemie.planat@mail.mcgill.ca)

**Abstract.** Mesoscale eddies are ubiquitous in the Arctic Ocean and are expected to become more numerous and energetic as sea ice continues to decline. Yet, the spatio-temporal characteristics of these eddies are poorly documented. Here, we apply an eddy detection and tracking method to ~~investigate mesoscale eddies in the Canadian Basin over the period 1995–2020 from the~~ the output of a high resolution (1/12°) regional model of the Arctic - North Atlantic ~~in order to investigate mesoscale eddies in~~

5 ~~the Canadian Basin over the period 1995–2020. Over that period, about 6,250 eddies are detected per year and per depth level and are 6000 eddies per year are detected in the surface layer, while about 9000 eddies per year are detected in the pycnocline layer, and about 5500 eddies per year in the Atlantic Waters (AW) layer. The eddy population is generally distributed about~~ equally between cyclones and anticyclones. ~~Yet, within the pycnocline and surface layer, a clear dominance of anticyclones over cyclones is found at the centre of the Beaufort Gyre, in line with observations from Ice Tethered Profilers (ITPs). The~~

10 ~~observed dominance of anticyclonic eddies reported by ITPs thus likely partially arises from the regional focus of the ITPs. On average, these eddies last 10 days, travel 11 km and have a radius of 12.1 km. These statistics hide strong regional and temporal disparities within the eddy population studied. In the top 85 m surface layer, the seasonal, decadal and interannual variability in the number of eddies and in their mean characteristics follow that of the sea ice cover. In contrast, below the upper pycnocline, the eddy within the pycnocline layer and below, the number and properties of eddies show a weakened seasonality. At all~~

15 ~~depths, eddy characteristics and generation rate the characteristics and density of the eddy population show a strong asymmetry between the slope and the centre of the Canadian Basin. The Over the slope, the upper 85 m show an increase in the number of eddies generated along the slope, while, while the pycnocline layer shows a net diminution of the number of eddies generated is visible within the pycnocline layer along the slope presumably due to the stabilizing effect of the slope. An. Within the AW layer, an increased number of eddies are is generated in the vicinity of the cyclonic boundary current in the AW layer. The vast~~

20 ~~majority of eddies have no temperature nor salinity signature with respect to their environment, although a significant portion of long-lived eddies, located along the Chukchi shelf break, have a non-negligible temperature anomaly and penetrate into the Beaufort Gyre, thus suggesting a mechanism for the penetration of heat into the gyre. The Over the 26 years analysed here, the number of eddies generated within the upper 85 m increases by 34% over the 25 year of simulation, with the largest increase occurring in the open ocean and marginal ice zone. The Marginal Ice Zone. Within the pycnocline layer, the number of eddies between the upper and lower pycnoclines increases by 45%, with a strong year-long increase in 2008, presumably in response~~

to the Beaufort Gyre spin-up in 2007-2008 ~~associated with the record low in sea ice extent~~. The number of eddies in the Atlantic Waters (AW) layer shows an overall increase of 41% ~~with, but~~ little interannual variability. ~~Finally, the analysis shows that the dominance of anticyclonic eddies within the Beaufort Gyre reported from measurements with Ice Tethered Profilers is partly due to a spatial sampling bias. This~~ We suggest that this model-based eddy census can thus help ~~interpret some of the discrepancies found between observational studies~~ investigate the recent changes in the dynamical equilibrium of the Beaufort Gyre by providing a consistent spatio-temporal characterization of mesoscale eddies in the Canadian basin ~~along the past two decades~~.

## 1 Introduction

Observations and numerical models reveal that mesoscale eddies are ubiquitous in the Arctic Ocean, including under sea ice (e.g. Manley and Hunkins, 1985; Cassianides et al., 2023; Liu et al., 2024). These eddies are thought to play an important role in the transport of heat, salt and nutrients from the shelves to the deep basins (Watanabe, 2011; Watanabe et al., 2014; Spall et al., 2008; Pickart et al., 2005) and possibly in the modulation of the ~~marginal ice zone (MIZ; Gupta et al., 2024; ?; Manueharyan and Thompson, 2022)~~ Marginal Ice Zone (MIZ; Gupta et al., 2024; Martínez-Moreno et al., 2025; Manucharyan and Thompson, 2022). In the Canadian ~~basin~~Basin, mesoscale eddies are also hypothesized to be a key component of the dynamical equilibrium of the large scale circulation through the dissipation of potential energy that accumulates within the anticyclonic Beaufort Gyre (BG, Manucharyan et al., 2016; Manucharyan and Spall, 2016; Meneghelli et al., 2020; Armitage et al., 2020). ~~Future projections of the Arctic show an increasingly energetic ocean with enhanced eddy activity (Li et al., 2024; von Appen et al., 2022) as the anticyclonic mean circulation gets stronger (Muilwijk et al., 2024) and sea ice gets thinner, less concentrated, and more mobile (Meredith et al., 2001; Meier and Stroeve, 2022). It thus appears important to document the spatio-temporal characteristics of mesoscale eddies in the changing Canadian Basin to further our understanding of the physical mechanisms controlling their generation and dissipation and of their role in the dynamics and tracer transport~~ Additionally, eddies possibly play a role in the build-up of the subsurface heat reservoir by driving the penetration of relatively warm summer Pacific Waters (sPW) within the gyre (MacKinnon et al., 2021; Spall et al., 2018; Planat et al., 2025). However, despite their possible role in the thermo-dynamical equilibrium of the BG, characteristics of the mesoscale eddy field and its evolution through time remain largely unknown in the Arctic, for one part due to the sparsity of observations, in particular under ice, and for another part due to the high resolution needed for models to represent the mesoscale at high latitude.

~~Over the past two decades, Ice Tethered Within the Canadian Basin, measurements with Ice-Tethered Profilers (ITPs; Toole et al., 2011) and moorings which were deployed as part of the Beaufort Gyre Exploration Project (<https://www.whoi.edu/beaufortgyre>) have enabled some characterization of mesoscale and submesoscale coherent eddies from either density and temperature anomalies (Zhao et al., 2014, 2016) or Potential Vorticity (PV) anomalies (Cassianides et al., 2023). The latter study reports  $\mathcal{O}(500)$  eddies from approximately 130,000 profiles across the Arctic the detection of  $\mathcal{O}(400)$  eddies between 2004 and 2019, among which 87% are in the Canadian Basin, with the majority lying (Zhao et al., 2014; Cassianides et al., 2023)~~

60 . The majority of these eddies were found to lie within the halocline (50-300 m). Eddies detected from PV anomalies within the top 700 m comprise 67% vortices with a cold core and 9% with a warm core. The documented eddies are predominantly anticyclonic (> 95%), a ratio also reported in Zhao et al. (2014). Radii are observed to range from 3-15 km for analyses based on ITP profiles and from 3-80 km for analyses based on mooring profiles. No seasonality in the number of eddies or in their properties is observed, and the discussion on the interannual variability is made difficult by the temporal variability of the number of ITP profiles across the last two decades. As opposed to the localized in-situ observations, satellite imagery offers a larger scale description of the eddy field based on surface signatures of eddies. Analyses of synthetic aperture radar data from , with a few detected at greater depth. Analyses of synthetic aperture radar data in 2007, 2011 and 2016 in the Western Arctic identify identified more than 7,500 eddies with diameters ranging from 0.5 km to 100 km, with cyclones twice as numerous as anticyclones, a result that strongly contrasts with the predominance of anticyclones observed from in-situ observations (Kozlov et al., 2019). In the same area within the seasonally ice-free and MIZ regions (Kozlov et al., 2019).  
70 Similarly, altimetry-based eddy detection reports detection within the seasonally ice-free region reported 2,000 eddies ranging from 20 to 60 km in radius between 1993 and 2018 , with orbital velocities ranging from 0.05 – 0.4 m s<sup>-1</sup>, and equally distributed between cyclones and anticyclones (Kubryakov et al., 2021). Finally, analyses (Kubryakov et al., 2021), an order of magnitude difference from in situ observations, likely due to the better spatial coverage of the ice free region and MIZ. Analyses of rotating ice floes with optical satellite images were also used to provide information about the eddy population  
75 within the MIZ of the Beaufort Gyre, revealing thousands of eddy-like signatures over the last two decades reveal order of thousands of eddy-like signatures having characteristic sizes ranging from 10 to 60 km with twice as many anticyclonic as cyclonic floes (Manucharyan et al., 2022). Contrasting characteristics between in-situ-based and satellite-based eddy datasets may arise from differences in the fields sampled including in particular the depth at which eddies are detected, with ITPs and moorings sampling from the near surface to 500-800 m while satellite-based observations can only report on features  
80 with a surface signature. Additionally, satellite observations of the eddy field are limited to the (Manucharyan et al., 2022). Even though no consensus was found in the eddy count across the different observational datasets, all satellite observations have shown regions densely populated with eddies over the continental shelf and slope, and in the open ocean and MIZ (Kozlov et al., 2019; Kubryakov et al., 2021), while in situ observations have demonstrated the presence of numerous eddies in the central basin below sea ice and at depth (Carpenter and Timmermans, 2012; Zhao et al., 2014; Cassianides et al., 2023).  
85

90 The density of eddy population as well as their spatial extents (both lateral and vertical), that mostly correspond to the shelf and shelf break areas. By design, ITPs can only sample the eddy field underneath the (pack)ice. These different observation approaches also lead to temporal biases, as, for instance, the MIZ is only found in summer in the BG. Contrasting eddy characteristics may also arise from the various detection methods used, which inherently sample different information, e.g. ITPs flowing "across" eddies vs moorings observing eddies passing by (Cassianides et al., 2023). Additionally, differences may also originate from biases due to the spatial resolution of instruments; e.g. altimetry-based detection are known to sample the larger and polarity, have provided hints at the processes driving eddy generation. In particular, the polarity has been scrutinized to better understand the hydrography and dynamics of eddies, but reconciling the picture provided by the

different observation datasets has proven difficult. While in situ observations show a predominantly anticyclonic eddy field (95) ( $> 95\%$  Zhao et al., 2014; Cassianides et al., 2023), in line with optical satellite imagery which finds twice as many anticyclonic as cyclonic floes (Manucharyan et al., 2022), altimetry shows an equally distributed polarity (Kubryakov et al., 2021), and synthetic-aperture radar imagery shows cyclones twice as numerous as anticyclones (Kozlov et al., 2019). Mechanisms of eddy generation were proposed to sustain the strong asymmetry documented from in-situ observations, such as subduction processes at outcropping fronts (Manucharyan and Timmermans, 2013) and baroclinically unstable coastal boundary currents (D'Asaro, 1988; Hunkins, 1974; Zhao et al., 2014). Furthermore, part of the mesoscale eddy spectrum only (Kubryakov et al., 2021) . Finally, some methods may be more sensitive to the detection of certain features. For instance, CTD cast-based and satellite-based detections of eddies more reliably detect anticyclones than cyclones, due to the stronger coherency of the former (Stegner et al., 2021; Giulivi et al., 2022). Overall, considering the sparsity of observations and their inherent biases, it remains challenging to have a fully coherent description of the eddy field from observations. Anticyclone to cyclone asymmetry may be attributed to the stronger coherency (100) and a slower decay of anticyclones, a characteristic reported for eddies at lower latitudes (Chelton et al., 2011), probably leading to an over-representation of anticyclones in eddy censuses (Stegner et al., 2021; Giulivi and Gordon, 2006). Contrasts between surface intensified and at depth eddies may also impact the statistics of eddy polarity, but this is yet to be shown.

Numerical models offer an alternative framework to investigate eddies and their characteristics by providing a consistent and (110) complete dataset, although they come with limitations and biases of their own. Idealized configurations of the BG and/or of the Alaskan boundary current exhibit vortex-like mesoscale features, on average weaker and larger than the ones detected from investigating eddy sizes, in-situ observations or satellites ( $\mathcal{O}(100)$  km, Manucharyan and Spall, 2016; Meneghelli et al., 2018a; Spall et al., 2022). It remains unclear, however, how to compare these idealized model-based results of the mesoscale eddy field with observations, in particular because these models have a limited representation of the processes that could generate mesoscale eddies (e.g., (115) they typically lack a mixed layer). Recently, observations have reported eddies across both the submeso- and meso-scales, with radii ranging from 3 to 15 km when detected from ITP profiles and from 3 to 80 km when detected from mooring profiles (Cassianides et al., 2023). The difference in the eddy size range may be attributed to the detection methods used; while ITPs flow "across" eddies, moorings observe eddies passing by (Cassianides et al., 2023). On the other hand, satellite observations have typically observed eddies with diameters ranging from  $\mathcal{O}(10)$  km up to  $\mathcal{O}(100)$  km (Kubryakov et al., 2021; Manucharyan et al., 2022) . (120) with synthetic-aperture radar images capturing features down to  $\mathcal{O}(1)$  km (Kozlov et al., 2019). Only recently has the resolution reached by realistic models become fine enough in the Arctic to resolve at least part of the mesoscale spectrum (Regan et al., 2020; Hu et al., 2019; Wang et al., 2020) in the Arctic, where the first Rossby radius of deformation varies between  $\approx 15$  km in the Canadian Basin and  $\approx 8$  km in the Eurasian Basin, down to 1 – 2 km on the shelves (Nurser and Bacon, 2013; Hu et al., 2022) . An analysis of the Eddy Kinetic Energy (EKE) in the entire Arctic Ocean in a 1 km resolution model shows peaks of EKE (125) at 400 m depth at spatial scales of around 60 km, with 50% . Further, this model shows that about half of the EKE is contained at scales smaller than 30 km (Liu et al., 2024), which corresponds to the upper boundary of the mesoscale range. In a 3 – 4 km resolution regional model, focusing on the Canadian basin, a peak of EKE is found in 2007–2008 in response to the anomalous wind forcing leading to the spin-up of the BG (Regan et al., 2020). However, these descriptions of the mesoscale

130 eddy field through the EKE offer a statistical integrated quantity only, and does not relate directly to individual features that are comparable to that detected from satellite or in situ observations.

135 On the vertical, eddies are found to form respectively at the surface, within the pycnocline layer, and at depth. The shallow eddies are confined to the upper surface layer by the strong stratification and have a vertical extent of typically 100 m, while eddies at depth can span up to  $O(1)$  km and are located around 1, 200 m (Carpenter and Timmermans, 2012). In between, double core eddies have been detected with a shallow core at the base of the pycnocline and a deep core within the Atlantic Water layer (Zhao and Timmermans, 2015). Idealized model configurations of the BG have shown vertical modes of baroclinic instabilities with similar vertical structure (Meneghelli et al., 2021). Overall, while observations have revealed different types and origins of eddies based on their dimensions and repartitions, the number of detected features has remained relatively low, hence preventing a systematic documentation of their spatial characteristics and geographical distribution that would allow for more robust statistics of the eddy population. The recent advent of fine resolution ocean-sea ice models has enabled such an investigation. Yet, it remains to be done.

140 In the Canada Basin, mesoscale eddy activity displays a strong seasonal cycle at the surface that is directly linked to that of sea ice (Hunkins, 1974; Meneghelli et al., 2021; Manucharyan and Thompson, 2022; Rieck et al., 2025b). In ice-free regions, thus mostly during summer, a vigorous mesoscale eddy activity is reported in both observations and models. In contrast, below sea ice, or more generally in winter, a quiescent surface layer is observed with eddies that last as short as a few days (Meneghelli et al., 2021). The short lifetime of under-ice eddies highlights the role of sea ice in dissipating eddy energy through friction. At subsurface though, eddies, shielded from the effect of sea ice by the strong stratification, may persist beyond months (D'Asaro, 1988; Hunkins, 1974). Subsurface eddy lifetime cannot be precisely estimated from observations, though, as both ITPs and moorings only capture a portion of the eddy trajectory.

145 150 As sea ice shrinks and the gyre intensifies in the Canada Basin, the number of mesoscale eddies is expected to increase. Satellite observations of spinning ice floes hinting at the eddy field have suggested such a trend over the past two decades (Manucharyan et al., 2022). Likewise, the number of eddies has been found to vary on interannual time scales with the intensity and freshwater content in the Beaufort Gyre (Kubryakov et al., 2021; Manucharyan et al., 2022; Zhang et al., 2016).

155 These observations tend to confirm the suggested role of mesoscale eddies in the gyre equilibration through the conversion of potential energy, which accumulates within the freshwater reservoir at the centre of the anticyclonic BG, into eddy kinetic energy. In the same line, modelling showed an enhancement of the EKE concurrent with the intensification of the gyre following increased wind forcing and sea ice retreat in 2007 (Regan et al., 2020). However, EKE was shown to only increase for a couple years in the model of Regan et al. (2020), thus questioning the mechanisms at play in the long-term equilibration of the gyre. In addition, to fulfil their role in the dynamical equilibrium of the gyre, Manucharyan and Stewart (2022) argue that eddies should be generated from baroclinic instabilities within the gyre, which cannot lead to strong polarity asymmetry in contrast to what is documented from ITP measurements. To reconcile this dynamical constraint with observations, Manucharyan and Stewart (2022) further suggest that both types of eddies exist in the BG. For one hand, small and cold anticyclones travelling freely from the shelfbreak, where they are generated through coastal boundary current instabilities or outcropping fronts (Manucharyan and Timmermans, 2022).

165 to the centre of the Gyre. For the other hand, larger and weaker eddies formed from baroclinic instability in the interior of the gyre that are yet to be observed from in-situ measurements.

Finally, the shrinking and thinning of sea ice that has been observed over the past decades and is projected to continue into the future (Meredith et al., 2001; Meier and Stroeve, 2022) will inevitably reduce the frictional dissipation of eddies, thus allowing more eddies to survive in the surface layer. The projections of the future Arctic with eddy-rich models show an increasingly energetic ocean with enhanced eddy activity in ice-free regions but also under sea ice (Rieck et al., 2025b; Li et al., 2024).

170 The enhanced eddy activity at the surface may drive more lateral mixing of heat with potential feedback on the ice. Likewise, changes in stratification may affect the eddy activity and characteristics. As suggested by Meneghelli et al. (2021), if the upper layer stratification were to weaken as the sea ice reduces, subsurface eddies that persist all year long shielded from sea ice by the strong vertical stratification may extend across reaching the surface. The evolution of the eddy characteristics over the Arctic in transition are yet to be investigated to foresee the upcoming changes in the eddy field and possible feedbacks on the ice 175 cover. ~~Additionally, by documenting the mesoscale transient eddy field through the analysis of the EKE, these studies take into account variability at all spatial scales, including large scale (but transient) features such as e.g. meanders of the mean currents.~~

Overall, no consensus has yet emerged on eddy characteristics in the Canadian Basin leaving large uncertainties that hamper robust projections of a future more energetic Arctic. In this paper, we propose a census of mesoscale ~~eddies (i.e. vortex-like features(eddies))~~ that develop in the Canadian Basin ~~along with a documentation of their spatio-temporal characteristics.~~ The Canadian basin is defined as the region between 69–85°N and 108–180°W, thus fully encompassing the BG and its surrounding area. Note that we also define the Canada Basin, abbreviated CB, between 73–77°N and 135–152°W, as a specific region of using a high-resolution regional model of the BG for analysis purposes (see Fig. 1). Arctic. To do so, we detect and track eddies to extract key properties such as size, lifetime, polarity and thermohaline anomalies. The resulting 185 eddy dataset comprises  $O(10^3)$  eddies/year thus enabling us to derive robust statistics on eddy properties. Besides, the dataset, which is fully coherent in space and time, is used to document changes of eddy characteristics between 1995 and 2020, hence covering a period of changes in strong ocean dynamical and sea ice state in the Canadian Basin. We perform a detection and tracking of eddies~~simulated by a 3–4 km regional model of the Arctic Ocean over the period 1995–2020. This census aims to facilitate the comparison with observations and the documentation of the eddy properties, and the implementation of the~~ 190 Lagrangian framework allows, the Lagrangian framework allowing to discuss the displacement of eddies within the basin. The paper is organized as follows. The model and the eddy detection and tracking algorithm are described in Section 2. The spatio-temporal eddy census is presented in Section 3. A discussion of key differences with observations is offered in Section 4 together with the main findings of this study and future perspectives.

## 2 Methods

195 In the rest of this paper, the Canadian basin is defined as the region between  $69\text{--}85^\circ\text{N}$  and  $108\text{--}180^\circ\text{W}$ , thus fully encompassing the BG and its surrounding area. Note that we also define the Canada Basin, abbreviated CB, between  $73\text{--}77^\circ\text{N}$  and  $135\text{--}152^\circ\text{W}$ , as a specific region of the BG for analysis purposes (see Fig. 1).

## 2.1 The pan-Arctic high-resolution model CREG12

### 2.1.1 Model and simulation

200 We use an updated version of the  $1/12^\circ$  regional Arctic-North Atlantic configuration CREG12 (Canadian Regional; Dupont et al., 2015). CREG12 ~~runs with is based on~~ the ocean modelling platform Nucleus for European Modelling of the Ocean (NEMO) version 4.2.2 (Madec et al., 2023) ~~and the Sea Ice modelling Integrated Initiative 3 (SI3) sea ice model, with levitating sea ice, five categories of ice and two layers of snow (Vancoppenolle et al., 2023)~~. The model is run on an ORCA12 seamless regional grid with horizontal resolution  $\approx 3\text{--}4\text{ km}$  in the central Arctic (Barnier et al., 2014). It uses a  $z^*$  vertical coordinate 205 with 75 levels spaced by 1 m at the surface and 150 m at 1500 m. This relatively fine horizontal grid size allows for an explicit resolution of ~~mesoscale eddies most of the mesoscale spectrum~~ within the deep basins where the first Rossby radius of deformation  $R_o$  is  $\approx 10\text{--}15\text{ km}$ , but not over the continental slope and shelf where  $R_o < 7\text{ km}$  (~~Nurser and Bacon, 2013~~).  
210 (~~Nurser and Bacon, 2013, see also Fig. S1, ).~~ Higher resolution simulations of the Arctic Ocean ( $\approx 1\text{ km}$ ) have shown that the EKE spectrum peaks around 50 km (Li et al., 2024) and that more than 80% (resp. 65%) of the EKE is contained in scales larger than 10 km (resp. 20 km; Liu et al., 2024). Therefore, we argue that  $1/12^\circ$  is a resolution fine enough to represent most 215 of the mesoscale features in the Beaufort Gyre and along its margins (but not over the shelves), while it runs at a cost that allows for decadal integration. This The configuration includes a ~~third-order third-order~~ momentum flux formulation, a ~~second order second-order~~ scheme for tracers advection, with an additional bi-Laplacian viscosity, diffusivity formulation depending on the local velocity, and a turbulence closure scheme for vertical mixing. The representation of tidal mixing effects is included 220 in the comprehensive parameterization of mixing by breaking internal tides and lee waves (De Lavergne et al., 2016).

~~The ocean component is coupled to the Sea Ice modelling Integrated Initiative 3 (SI3) sea ice model, with levitating sea ice that uses five categories of ice and two layers of snow (Vancoppenolle et al., 2023)~~. The simulation is initialized in 1979 from the World Ocean Atlas 2009 for temperature (Levitus et al., 2010) and salinity (Antonov et al., 2010) with the ocean at rest and is run until 2020. Sea ice conditions are initialized from the Pan-Arctic Ice Ocean Modeling and Assimilation System 220 (PIOMAS) (Zhang and Rothrock, 2003). The ocean and sea ice are forced with hourly atmospheric fields from the European Centre for Medium-Range Weather Forecasts Reanalysis version 5 (ERA5, Hersbach et al., 2020). ~~To compensate for the known warm biases of ERA5 at the sea surface (e.g. Batrak and Müller, 2019), the snow conductivity is set to  $0.5\text{ W/m/K}$ , the ice-ocean drag coefficient to  $7 \cdot 10^{-3}$ , the atmosphere-ocean drag coefficient to  $1.2 \cdot 10^{-3}$ , and the ice strength to  $2 \cdot 10^{-4}\text{ N m}^{-2}$ .~~ The open boundary conditions at Bering Strait and along  $27^\circ\text{N}$  in the Atlantic are specified daily from the output of 225 GLORYS12V1, a global reanalysis at  $1/12^\circ$  resolution run from 1993 to 2020 (Lellouche et al., 2018). Prior to 1993, output of GLORYS12V1 between 1993 and 2021 ~~are is~~ used to build a climatology and force the open boundaries of CREG12. At Bering Strait, meridional velocities are adjusted to constrain the inflow to about ~~1.4 Sv, a value close to observations~~

1.1 Sv, matching observation estimates (Woodgate, 2018). The river run-off and Greenland melting are specified from the HYDRO re-analysis (Stadnyk et al., 2021) following Weiss-Gibbons et al. (2024). An additional sea surface salinity restoring 230 with piston velocity of 167 mm day<sup>-1</sup> is implemented in ice-free regions at monthly frequency using the World Ocean Atlas 2009 (Antonov et al., 2010). For additional details on the run, the reader is referred to Talandier and Lique (2024).

### 2.1.2 Evaluation of the simulation

We present here a brief evaluation of the model's representation of the hydrography, circulation and sea ice conditions in the Canadian Basin. For a more in-depth assessment of the model's performance, the reader is referred to Regan et al. (2020) and 235 Barton et al. (2022) who use similar configurations. In this study, we focus on the period 1995-2020 to let the model equilibrate between 1979 and 1994. Over the period of analysis, the mean September sea ice cover concentration is comparable to that derived from satellite observations (Fig. 1a,b) with small differences in summer on the Eurasian shelf and a low bias in the western CB. The modelled geostrophic circulation (Fig. 1a,b). On average across the Arctic and along the simulation, the sea ice extent deviates from that derived from satellite observations by -7% in September and -16% in March. When compared to the 240 PIOMAS Arctic Sea Ice Volume Reanalysis (Zhang and Rothrock, 2003), the sea ice thickness is 35 cm thinner in September and 20 cm thinner in March (Fig. S2b, S3b). The interannual variability of sea ice extent is well captured by the model across the 26 years of simulation. A strong decline in sea ice starting around 2000 and persisting in time appears in the model in agreement with observations (see Fig. S2c, S3c in supplementary). The corresponding location of ice loss is generally well represented despite some biases in the ice concentration along the Eurasian shelf in summer and high biases along Yermack 245 plateau and Greenland eastern shelf in winter (see Fig. S2a,b, S3a,b in supplementary).

The geostrophic circulation of the model at the surface, related to estimated through the gradients of Sea Surface Height (SSH, Fig. 1c,d), shows comparable pattern and intensity than as observations for the BG (anticyclonic) and for the circulation in the Nansen Basin (cyclonic, Fig. 1e,f). Within the CB, CREG12 successfully presents the vertical distribution of temperature extrema associated with the three main water masses present in this region (Fig. 1e,f), namely the summer Pacific Waters (sPW; temperature maximum at 100 m), the winter Pacific Water (wPW; temperature minimum at 200 m), and the Atlantic Water (AW; temperature maximum at 550 m). Small biases in the magnitude of the temperature extrema themselves (warm bias for the wPW, and cold bias for the sPW and AW) are noted. Despite a high salinity bias at the surface in CREG12, the modelled stratification, that allows and sustains this vertical temperature structure, displays the so-called "bowl shape" of the BG visible through the tilted isopycnals along the edges of the gyre, although slightly weaker in the northernmost side of the BG in CREG12. The model offers overall a reasonable overall fresh water content, referenced to 34.8 psu, shows a strong increase between 2003-2009 in the Canadian Basin as documented from the Beaufort Gyre Exploration Project (Proshutinsky et al., 2009) followed by a plateau (see Fig. S4 in supplementary).

Overall, the model offers a realistic representation of the main circulation features, with the anticyclonic BG extending down to  $\approx 250$  m and intensifying along the Chukchi shelf break (see the Mean Kinetic Energy (MKE) in Fig. ??S5). The cyclonic 260 boundary current within the AW layer is found around the CB at 500 m with a returning branch of weaker intensity along the Canadian Archipelago (Fig. ??eS5c). Upper outflows through the Canadian Archipelago are similar to observation-based de-

rived circulation (see Fig. ??, see also ?). Analyses of EKE shows an intensification (see Fig. S5, see also Planat et al., 2025). Climatologies of EKE computed relative to monthly means show larger values along the shelf break and along topographic features such as Northwind Ridge(NWR) , with amore quiescent deep basin by , both at the surface (not shown) and within the pycnocline (Fig. 2a). In contrast, the deep basin is more quiescent, with EKE one to two orders of magnitude ,in line with lower than on the shelves (Fig. 2a,b.). The shelf-deep basin contrast in EKE magnitude is a typical feature of the mooring-based estimates of EKE (Fig. 2a,b, see also von Appen et al., 2022) (von Appen et al., 2022). Yet, the intensity of EKE is about one order of magnitude smaller in our model than that derived from observations (von Appen et al., 2022), as documented previously in Regan et al. (2020). The MKE, which captures the location of the main currents, is of similar order of magnitude as in observations (von Appen et al., 2022), with discrepancies being partly attributed to the difference in the exact locations of the main currents between models and observations (Fig. S5). Finally, the vertical structure of the total kinetic energy is similar to that derived from the Beaufort Gyre Exploration Project Moorings (compare Fig. S6 with for instance Fig. A1 from Meneghelli et al., 2019, with sub-surface intensified structures between 30-200 m, and deeper (although weaker) structures between 400-2000 m, as evidenced in observations by Carpenter and Timmermans (2012)).

## 275 2.2 Detection and tracking of mesoscale eddies

### 2.2.1 Detection

We perform an offline detection and tracking of mesoscale eddies within the Canadian Basin over 1995-2020. Our definition of *eddies* spans here a broad range of mesoscale rotating features, from the evanescent vortices quickly dissipated by sea ice to the more persistent features that may eventually evolve into materially coherent vortices. This broad definition thus includes 280 parts of the "turbulent soup" that is expected to develop at the surface in response to the atmospheric and ice forcings and should be captured by the model. Though short-lived, these features which are characteristic of the surface ocean, deserve an investigation as they allow to ~~investigate~~ examine the energy dissipation exerted by sea ice and participate to the ~~energetie~~ *dynamical* equilibrium of the basin. In the following, we focus on features with characteristic sizes from  $R_0 \approx 10$  km to  $2\pi R_0 \approx 60$  km (defining the mesoscale, e.g. Tulloch et al., 2011).

285 To identify eddies, we use the *eddytools* python package documented in [?Rieck et al. \(2025a\)](#). Eddies are detected using the Okubo-Weiss parameter (OW; Okubo, 1970; Weiss, 1991), which measures the relative importance of shear and strain to vorticity (Fig. 3a) in the velocity field:

$$OW = (\partial_x u - \partial_y v)^2 + (\partial_x v + \partial_y u)^2 - (\partial_x v - \partial_y u)^2 \quad (1)$$

where  $u, v$  denote the velocities along the  $x$  and  $y$  directions of the grid, locally orthogonal. The resulting OW field (Fig. 3b) is 290 compared to the local OW standard deviation ( $\sigma_{OW}(x, y)$ ) averaged over the full time period (Fig. 3c).  $\sigma_{OW}$  is computed over a  $L_\sigma \times L_\sigma$  box,  $L_\sigma$  being chosen small enough to capture the regional differences between e.g. the centre of the gyre and the boundary currents, but large enough so that  $\sigma_{OW}$  is not impacted by individual eddies. To be retained, eddies have to meet the

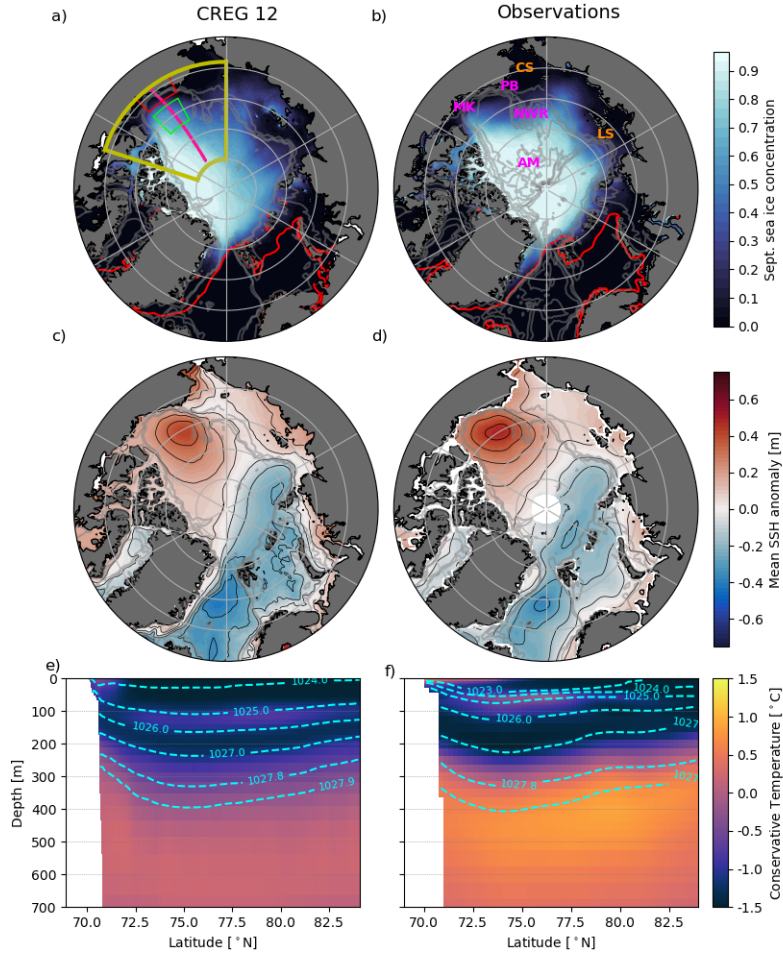


**Figure 1.** Mean sea ice concentration in September (background color) and in March (80 % contour in red) over 1995-2020 from (a) CREG12 and (b) National Snow and Ice Data Center (NSIDC) Climate Data Record (DiGirolamo et al., 2022), a blend between the NASA-Team algorithms (Cavalieri et al., 1984) and the NASA Bootstrap algorithm (Comiso, 1986). Mean Sea Surface Height (SSH) anomaly with respect to the mean over 2011-2020 and above  $65^{\circ}\text{N}$  from (c) CREG12 and (d) the updated altimetry-based product of Armitage et al. (2016). Black contours are evenly spaced every 0.1 m between  $-0.75\text{ m}$  and  $0.75\text{ m}$ . Mean conservative temperature (background) and potential density referenced to surface (dashed contours) along a transect at  $-145^{\circ}\text{E}$  over 2005-2014 from (e) CREG12 and (f) World Ocean Atlas 2023 climatology (Locarnini et al., 2024; Reagan et al., 2024). Note the different periods displayed for each variable to match that of the observation datasets. Boxes on panel a) represent the regions used for our analyses corresponding to the Alaskan shelf area (red) and the Canada Basin (green). The thick yellow box indicates the Canadian Basin i.e. the entire domain analysed in this study. The pink line is the section used for Fig. ??S9. In panel b), CS and LS stand from Chukchi and Laptev Sea, respectively, and NWR, PB, AM and MK for Northwind Ridge, Pt. Barrow, Alpha-Mendeleev Ridge and McKenzie River respectively. Thin gray lines show the bathymetry, respectively 100, 500 and 1000 m depth isobaths on (a), (c), (d) and 100, 500, 1000, 2000 and 3000 m depth isobaths on (b).

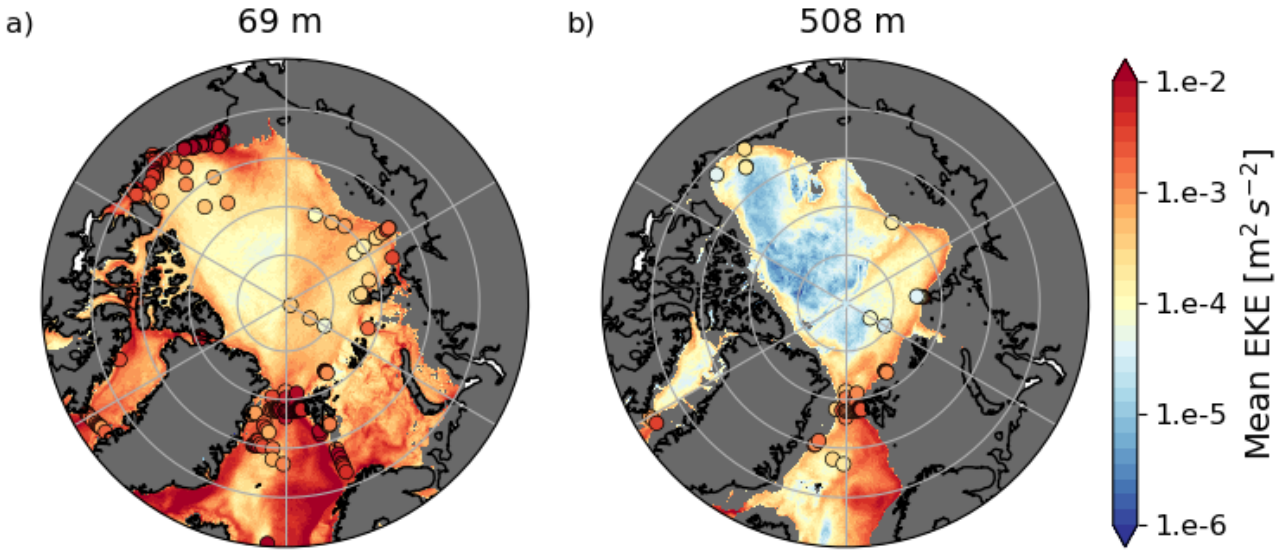


**Figure 2.** Eddy Kinetic Energy (EKE) computed from velocity anomalies with respect to the monthly means in CREG12 and averaged over the 26 years of simulation (a) at 69 m (within the halocline) and (b) at 508 m (within the AW layer). Super-imposed are mooring-based estimates of EKE from von Appen et al. (2022), computed similarly from monthly mean anomalies with fourth-order Butterworth filter with 2-day to 30-day cutoffs. The reader is referred to von Appen et al. (2022) for exact calculation method.

following condition :

$$OW(x, y, t) < -\alpha \sigma_{OW}(x, y) \quad (2)$$

295 where  $\alpha$  is a threshold value typically chosen between 0.2 and 0.5 (Isern-Fontanet et al., 2003; Chelton et al., 2007; Pasquero et al., 2001; ?)

As we aim to detect any vortex-like features that may develop in the Canadian Basin, including those which are not materially coherent, we choose a Eulerian over a Lagrangian approach for detection. The OW-method is based on velocities ( $u, v$ ) and thus preferable over SSH-based methods for detection in sea ice-covered areas where SSH-based detections are known to miss 300 objects that do not have a surface expression. Additionally, the OW-method has the advantage to be computationally efficient and thus seems well-suited for a detection run for 26 years at each model level between the surface and 1200 m. A comparison of our OW-based detection with those from Nencioli et al. (2010,  $u, v$  - based) and Chelton et al. (2011, SSH-based) was performed by Rieck et al. (2025a, see their Fig. S3). They show that the OW-based method detects higher numbers of eddies compared to the other methods, mostly due to its capability to detect weak eddies, i.e. eddies with small rotational velocities and SSH 305 anomaly. This detection bias towards weak eddies is commented in the discussion section.

The detection is implemented using daily-averaged output in the Canadian Basin. The detection and is run for each vertical level of the model independently above 1200 m (which represents a lower bound of the AW layer), totalling

49 levels. ~~Connecting~~ No 3D representation of eddies is attempted here as connecting the results between the vertical layers is not trivial and no 3D representation of eddies is attempted here, and would require a substantial development of the detection 310 and tracking algorithms. A brief evaluation of the vertical structure of eddies is however proposed in Section 3.1.1. Note that because  $\sigma_{OW}$  is computed independently for each depth level, the minimum OW used to identify an eddy also varies with depth. In other words, at depths of intense mesoscale activity, the OW an individual eddy needs to ~~have to be identified as such~~ ~~will be more extreme~~ be identified is higher. For each eddy, we estimate its radius with  $R = \sqrt{\text{area}/\pi}$  even though the eddies might have an elliptic shape.

315 We set the smallest eddies that the algorithm detects to occupy 20 grid points, which correspond to equivalent circular eddies with a minimum of 5 grid points across the diameter. A 5-grid point diameter circular structure corresponds to an eddy of 7.5 to 10 km radius, depending locally on the grid size of the model, which is the lower bound of  $R_0$  over the deep part of the Canadian Basin (see Nurser and Bacon, 2013). ~~On~~ ~~Over~~ the shelf, ~~where~~  $R_0$  is smaller ( $\approx 2 - 5$  km) ~~thus~~, we only detect the largest ~~of the~~ mesoscale rotating features. Statistics presented here include all detected features, but remain valid when filtering 320 out eddies on the shelf, as the vast majority of eddies are detected over the continental slope and within the basins (not shown).

Sensitivity tests for  $\alpha$  show that the vertical distribution of the ~~metrics investigated, that are~~ mean eddy radius, duration, 325 polarity ( $r_{C/T}$ , ratio of cyclones to total number of eddies) and ~~vorticity~~  $\Omega$  a proxy for the vorticity  $|\Omega|$  (see Sect. 2.2.3), are robust to changes of  $\alpha$  from ~~0.5 to 0.1~~ ~~despite to 0.5~~. Yet, we note changes in the total number of detected features with slightly larger, weaker and shorter eddies for smaller  $\alpha$  (Fig. ??S7). For our analyses, we ~~choose~~ choose  $\alpha = 0.3$  as an intermediate, ~~and commonly used~~, value. The box length  $L_\sigma$  over which to compute  $\sigma_{OW}$  needs to be tuned to the main spatial scales of ~~energy~~ ~~dynamical~~ regimes in the basin. In other words,  $L_\sigma$  should be small enough to capture the jet-like circulation along the Alaskan and Chukchi slopes that are about 200 – 300 km large, and large enough to allow statistically relevant values of  $\sigma_{OW}$ . We ~~argue~~ ~~found~~ that  $L_\sigma = 200$  km is a reasonable value to resolve the different dynamical regimes within the Canadian 330 Basin. Similarly to  $\alpha$ , sensitivity tests indicate that changing  $L_\sigma$  within the range [50, 400] km does not modify the vertical distribution of the mean eddy radius, duration, vorticity and polarity although the total number of detected features vary (not shown). Overall, modifications of  $\alpha$  and  $L_\sigma$  impact the precise definition of particular eddies but not the statistical properties of the eddy field.

## 2.2.2 Tracking

Eddies are tracked over consecutive days using three main criteria: (i) their speed of propagation, (ii) their polarity, and (iii) 335 their radius  $R$  (Fig. 3c). For each eddy detected on day  $t$ , if an eddy with similar radius (within  $[0.5R, 1.5R]$ ) and same polarity lies within a search radius  $R_s$  on day  $t+1$ , it is chosen as a continuation of the track. In case there is more than one eddy matching these criteria, the one ~~with the centre~~ located the closest to the original eddy's ~~centre~~ is chosen. Results do not appear sensitive to ~~the choice of~~ a search radius  $R_s \in [15, 53]$  km, and we choose a search radius  $R_s = 22$  km corresponding to a propagation speed of 25 cm/s, which is approximately the speed of the fastest simulated current within the domain, located 340 along the Chukchi slope in summer.

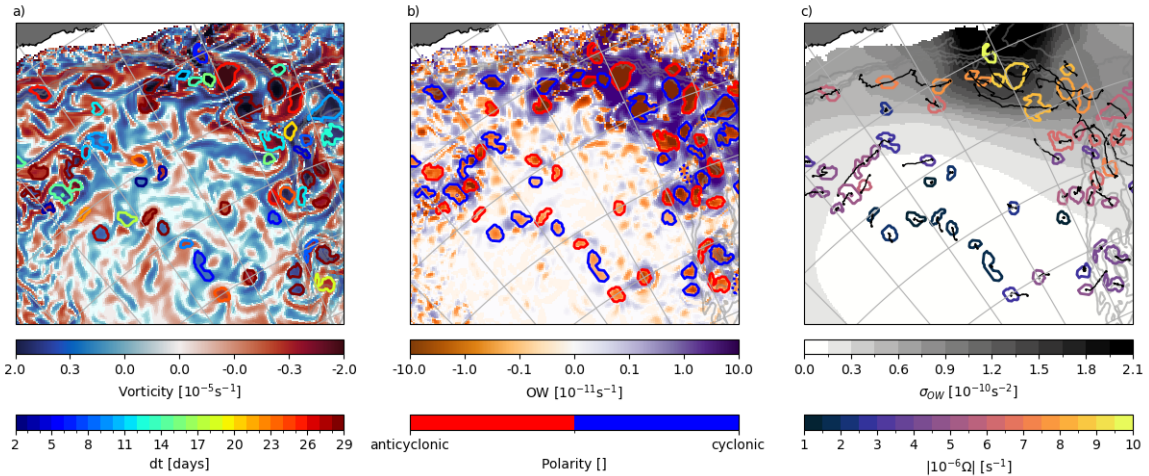


**Figure 3.** Example of detection and tracking of mesoscale eddies along the south-eastern edge of the CB at 30 m on Sept. 16th, 1996. Shown are: (a) the vorticity ( $= \partial_x v - \partial_y u$ ), (b) the OW parameter, and (c) the OW standard deviation  $\sigma_{OW}$  for one day in September chosen randomly (here, Sept. 16th, 1996) at 30 m along the south-eastern edge of the CB. Superimposed on each panel are contours indicating the detected eddies present on that day detected by the algorithm, coloured according to (a) their duration, (b) their polarity (red indicating anticyclones and blue cyclones), and (c) their intensity i.e. the absolute value of the difference between the vorticity in the centre of the eddy and the average vorticity along the edge of the eddy. Plain contours on (a), (b) and (c) indicate eddies lasting more than 2 days, dotted red and blue contours on (b) indicate eddies with a duration of one day. Black thin lines on (c) indicate the eddy trajectories. Thin gray lines indicate the 100, 500, 1000 and 1500 m depth isobaths.

The radius, location and grid-point occupied by each individual eddy are stored every day. We consider 345 assume eddies to be born (generated) the first time they are detected and to be dead (dissipated) the last time they are detected. However, the algorithm may occasionally lose track of eddies, leading to a given eddy being counted as two successive eddies of similar properties. This interruption in the tracking generally occurs with weak features that are not well developed and thus not detected as eddies over consecutive days. We remove these eddies by filtering out any eddy that does not persist over at least two consecutive days. While this filtering does not fully overcome the interruption in the eddy detection – in particular if one eddy splits into two different ones, or equivalently if two eddies merge – it removes most of the issue and enables us to focus more on well-developed eddies. Still, the majority of eddies we detect are relatively weak and have a duration shorter than their turnaround time scale (defined as the time it takes for a water parcel to do a full revolution,  $\tau = 2\pi/|\Omega|$  350 (i.e. an approximation of the expression suggested by Smith and Vallis, 2001, that is  $\tau = 2\pi/\zeta_{rms}$ , where  $\zeta_{rms}$  is the root-mean-square v

. A discussion of the characteristics of the more vigorous and persistent eddies ~~that are likely more comparable to the accepted definition of coherent mesoscale eddies~~ is proposed in Section 4.

### 2.2.3 Properties

For each detected and tracked eddy, we extract ~~or compute its absolute salinity ( $S$ ), conservative temperature ( $T$ ), and its~~ 355 intensity, that we define as the absolute vorticity amplitude of the eddy, i.e. the difference between the vorticity in the centre of the eddy and the average vorticity along the edge of the eddy ( $|\Omega|$ ). We equivalently report its relative intensity  $|\Omega|/f(\lambda)$  where  $f$  is the Coriolis parameter computed as a function of ~~the~~ latitude  $\lambda$ . ~~We also extract the mean By spatially averaging over the eddy area, we also extract its absolute salinity ( $S$ ), conservative temperature ( $T$ ), and the mean sea~~ ice concentration  $A$  and thickness  $h$  above each eddy ~~for each day~~.

360 Eddy properties are computed ~~by spatially averaging over the eddy area and are~~ and tracked along the eddy pathway. Except where mentioned, properties are extracted at the eddy generation time. ~~Localizations~~ Locations of eddies are obtained from their centre of mass - thus, the distance travelled by a given eddy between two consecutive days is possibly smaller than the grid resolution if an eddy is very slow. The properties of the eddy environment are defined by spatially averaging over a box that we take to be  $n = 3$  times larger than the ~~fitted~~ eddy width and length (thus not of identical size along both  $x$  and  $y$  365 directions) and from which we remove the eddy area. We note  $\Delta X = X_i^{eddy} - X_i^{env}$  the anomaly of property  $X$  at the time of eddy generation  $i$ . If two eddies develop next to each other, they will become each other's environment as we do not use a 2D eddy mask. To increase the robustness of the ~~anomaly quantification, we only report the anomalies when "significant" in the rest of the manuscript, except if mentioned~~. We define "significant" from the results, only significant anomalies are reported, 370 ~~except where mentioned otherwise. We first define the deviation  $\delta X$  from the environment noise using the~~ standard deviation of ~~property  $X$  over the environment removing~~ across the environment (i.e., excluding the eddy area),  $\sigma_X^{env}$  :

$$\delta X = \underline{\Delta X_i^{eddy} - X_i^{env}} + \begin{cases} +\sigma_X^{env} & \text{if } \Delta X < 0 \\ -\sigma_X^{env} & \text{if } \Delta X > 0. \end{cases} \quad (3)$$

~~The anomaly is said significant if  $\delta X$  and the anomaly  $\Delta X$  are~~ Then, the anomaly  $\Delta X$  is said *significant* if it is of the same sign as  $\delta X$ , that is if the anomaly is larger in absolute than the standard deviation over the area.

375 Finally, the normalized amplitude of the seasonal cycle is defined for each property  $X$  as:

$$SC_X = \frac{X_{max} - X_{min}}{\overline{X}} \quad (4)$$

where the maximum, minimum and mean are taken along the seasonal cycle.

	Radius $R$	Duration $dt$	Distance travelled $D$	Intensity $ \Omega $	Temperature anomaly $\Delta T$	Salinity anomaly $\Delta S$
10 <sup>th</sup> perc.	9.8 km	2 day	0.6 km	$5.7 \cdot 10^{-7} \text{ s}^{-1}$	-0.10°C	-0.25 psu
90 <sup>th</sup> perc.	15 km	21 days	26 km	$1.1 \cdot 10^{-5} \text{ s}^{-1}$	0.20°C	0.24 psu

**Table 1.** Eddy characteristics defined from the 10<sup>th</sup> and 90<sup>th</sup> percentiles of the distribution for all eddies at all depths above 1,200 m. Percentiles of the temperature and salinity anomalies are computed on  $\approx 15\%$  of the total eddy population.

### 3 Results

#### 3.1 Characteristics of mesoscale eddies at ~~basin-scale~~annual and seasonal scales

##### 380 3.1.1 ~~Across the Canadian Basin~~

Over 1995-2020, ~~and on average along the vertical~~, we detect and track about ~~6,250 eddies per model depth level and per 6,000 eddies per year~~ in the Canadian Basin. ~~Here, we present the statistics aggregated over the whole 1995-2020 period and over all depth levels above 1,200 m, hence accounting for the same eddy several times if that eddy spans several depth levels~~ This large number opposes the very few vortices detected from in-situ observations below the ice ( $\mathcal{O}(10)$  eddies per year, Cassianides et al., 2023; Zhou et al., 2023). ~~It is, however, closer to numbers reported from satellite observations in the MIZ or the Open Ocean (up to  $\mathcal{O}(1000)$  eddies per year, Kubryakov et al., 2020)~~ Most of the eddies detected in the model have a radius similar to the Rossby radius of deformation ~~with~~ ( $\bar{R} = 12.1 \text{ km}$ ), are short lived with an ~~averaged~~ duration  $\bar{dt} = 10$  days and do not travel far with an ~~averaged~~ distance travelled  $\bar{D} = 11.1 \text{ km}$  (Fig. 4a-c). Of all eddies detected, 49% are cyclones. Cyclones and anticyclones have a similar intensity ( $|\bar{\Omega}| = 4.6 \cdot 10^{-6} \text{ s}^{-1}$  corresponding to a relative intensity of  $|\bar{\Omega}|/f = 0.03$ ; Fig 4b). ~~Temperature and salinity anomalies are found for~~ The eddy intensity, lifetime and travelled distance have a standard deviation of the same order of magnitude as the mean. In particular, the distribution of the distance travelled shows three peaks in the distribution (Fig. 4b): a first one corresponding to quasi-stationary eddies, and two secondary ones centered around 4 km and 8 km. 15% of the eddies ~~show temperature and salinity anomalies with respect to their environment~~ (Fig. 4e,f). The narrow and short tail of the statistical distribution of ~~radius~~  $\Delta S$  indicates that the overwhelming majority of detected eddies have properties close to the mean, while the wider distribution of  $\Delta T$  indicate ~~relatively~~ large temperature anomalies for a significant portion of the eddy population (see box whiskers on Fig. 4 and ~~the 10<sup>th</sup> and 90<sup>th</sup> percentiles in~~ Table 1 ~~with numerical values of 10<sup>th</sup>/90<sup>th</sup> percentiles of each property~~). ~~The eddy intensity, duration and travelled distance have a standard deviation of the same order of magnitude as the mean. The distribution of the distance travelled, in particular, shows three modes (Fig. 4b): a first one corresponding to quasi-stationary eddies, and two secondary ones centered around 4 km and 8 km.~~ Interestingly, eddies with properties at the tail of the distributions do not represent a distinct population of eddies. For instance, larger eddies do not systematically live longer (see Fig. ??- S8).

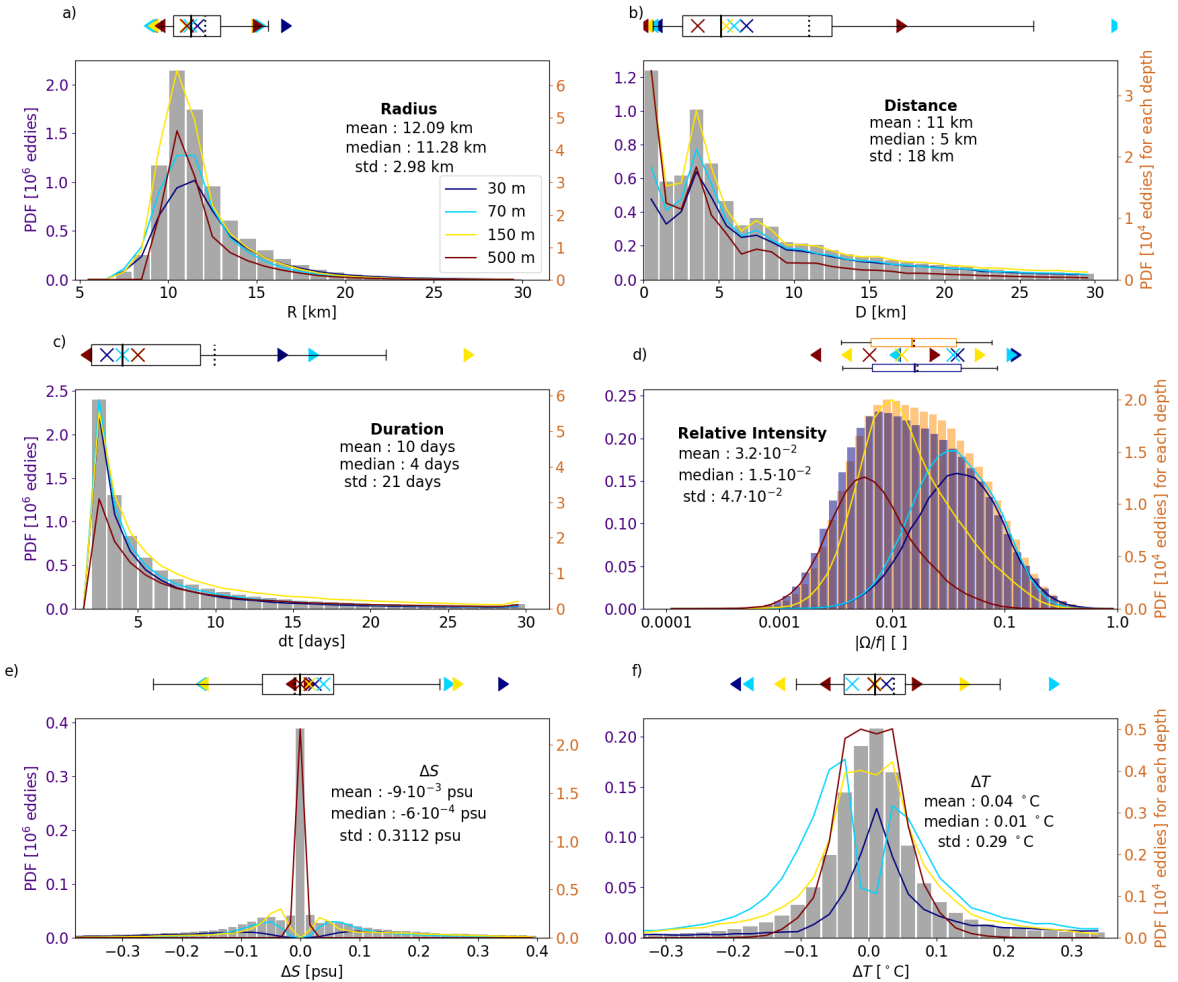


**Figure 4.** Histogram of the properties of eddies generated at all depths in the model: (a) radius, (b) distance travelled, (c) duration, (d) relative intensity for cyclones (blue) and anticyclones (orange), and anomalies in (e) salinity and (f) temperature with respect to the surrounding environment (see Sect. 2). All variables are estimated at the time of eddy generation, that is the first time an eddy is detected. Number of eddies are reported in million along the left axis (indigo). Anomalies are only accounted for when significant (see Sect. 2), that is only  $\approx 15\%$  of **all eddies are the eddy population is** considered for panels (e) and (f). Box plots indicate the quartiles Q1 and Q3, the median (plain line) and mean (dotted line), and the 10<sup>-th</sup> and 90<sup>-th</sup> percentiles in the whiskers. Plain lines correspond to the histogram of properties at specific depths (11 m, 30 m, 69 m, 147 m and 508 m), reported along the right axis in tens of thousands of eddies (orange). On panel d), plain lines report the histogram of absolute relative intensity, that is, for both cyclones and anticyclones together. Coloured  $\blacktriangleleft$ ,  $\triangleright$  and  $\times$  respectively indicate the 10<sup>-th</sup>, 90<sup>-th</sup> and median at the corresponding depth.

Statistics So far, we have presented the statistics of eddy properties aggregated over the whole eddy population hide significant differences across depth. Indeed, the general shape of the distribution of eddy properties is similar at all depths, but the means and percentiles vary (1995-2020 period and over all depth levels above 1,200 m, hence accounting for the same eddy several times if that eddy spans several depth levels. Yet, eddies may span over tens of meters to kilometres in the CB (Carpenter and Timmermans, 2012; Zhao and Timmermans, 2015). We observe some vertical coherency when looking at a few structures individually, in particular for structures spanning the pycnocline between 70-250 m, or surface intensified eddies, or eddies spanning the whole water column below 200 m (Fig. 5). This vertical structure is to vertical structure obtained from observations (Carpenter and Timmermans, 2012; Zhao and Timmermans, 2015) or predicted from baroclinic instability estimate (Meneghelli et al., 2021) in the CB. Therefore, statistics computed over the whole eddy population hide significant differences across depth (see the coloured plain lines and  $\blacktriangleleft$ ,  $\blacktriangleright$  and  $+$  in Fig. 4), motivating the analysis of eddy properties with depth. To this end, we seek to define vertical layers with consistent properties. Within the top 1200 m, the total number of eddies generated at each model depth level remains roughly constant between the surface and 85 m, and below 225 m, but increases by two thirds between 85 m and 225 m (Fig. 6a). We also note important transitions in the ratio of anticyclones versus cyclones, radius and eddy durations around these depths suggesting different mechanisms of formation and dissipation. On average across the basin and along the 26 years, these transition depths correspond to the upper pycnocline ( $\sim 85$  m) which is associated to the depth at which are found the summer Pacific Waters (sPW), and to the lower pycnocline ( $\sim 225$  m) which is associated to, and the winter Pacific Waters (wPW,  $\sim 225$  m, see Fig. 6g,h). Based on these depths, forming together the pycnocline layer.

Based on the evolution of the statistical properties with depth, together with the observation of the coherent structures with finite depth extent, we thus define three layers : the upper layer (0-85 m), the pycnocline layer (85-225 m) and the AW layer (225-1200 m). Next, we describe the eddy properties and discuss their formation and dissipation within each of these three layers. The results presented in the following are robust to the exact definition of the layer boundaries ( $\pm 2$  depth levels).

### 3.2 Characteristics of eddies within the surface layer

#### 425 3.1.1 Within the upper layer

#### 3.1.2 Mean-annual and seasonal cycle of eddy characteristics

Within the top 85 m, a total of  $\approx 6000$  eddies per year and per depth level are detected about 6000 eddies are detected every year. The properties of these eddies show a marked seasonal cycle (Fig. 6) that mainly follows that of the sea ice cover. Note that because we only track eddies in the horizontal and not in the vertical, we cannot discriminate eddies generated within the upper layer only from eddies extending across the upper and pycnocline layers. From winter to summer, the number of eddies increases by a factor of 10 with a minimum in April, just before the onset of sea ice melting, and a maximum in September when sea ice is at its minimum (Fig. 6a). The Mixed Layer (ML) depth – computed as the depth at which the potential density has increased by  $0.01 \text{ kg m}^{-3}$  compared to the potential density at 1 m – decreases from 35 m in January-May to 3 m in July, and increases from August to December, when it recovers 30 m (see also the stratification on Fig. 6h). The

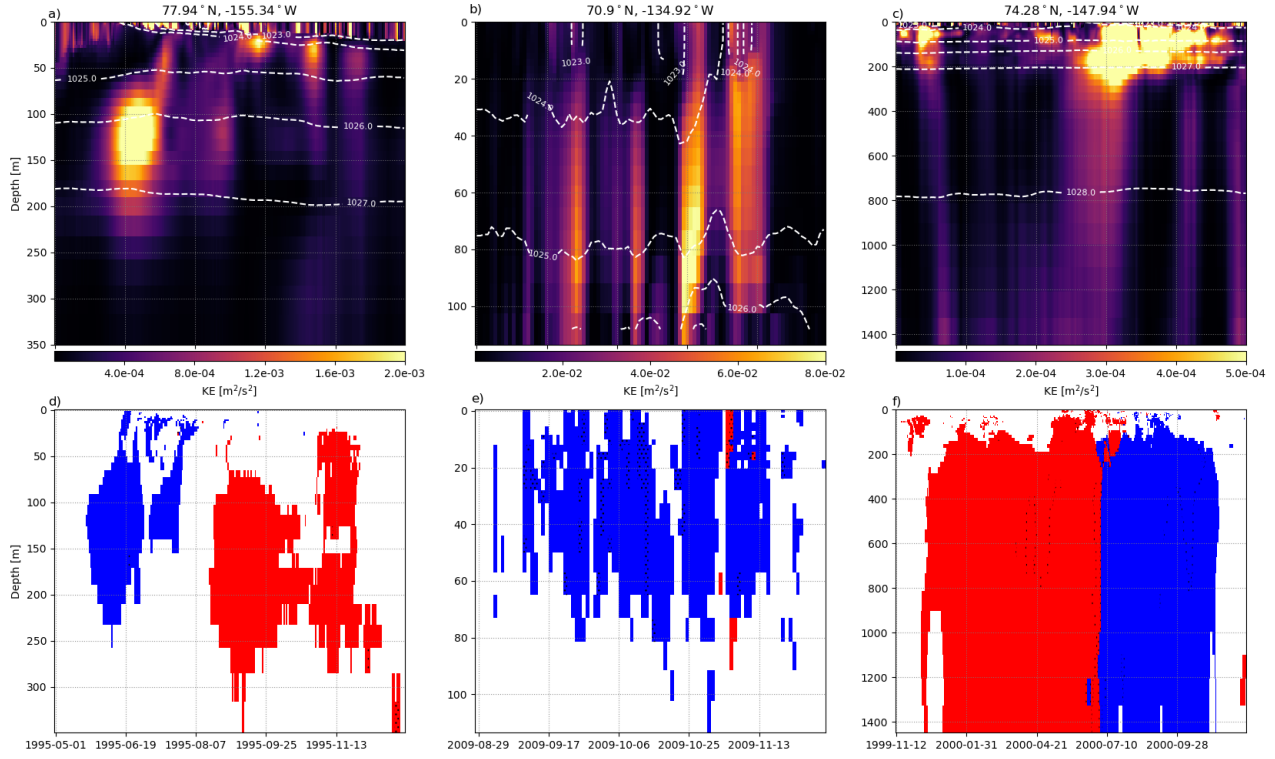


**Figure 5.** Daily averaged total kinetic energy (upper row) of a *virtual* mooring located at 77.94°N, -155.34°W (first column), at 70.9°N, -134.92°W (second column) and 74.28°N, -147.94°W (last column). Dashed white lines correspond to surface referenced isopycnals ( $\sigma_0$ ). Polarity of eddies passing by the virtual mooring (second row) and identified by our algorithm with cyclones in blue and anticyclones in red. White means no eddy detected. Dots (.) indicates an interruption in the tracking, meaning that the algorithm identifies a newly born eddy.

435 change in stratification associated to the ML depth delimits different regimes of variations for the mean radius, polarity and intensity. Within the ML, the averaged radius of eddies increases from 12 km in early summer to 14 km in fall, while below the ML, the averaged radius of eddies barely changes comparatively (increase from 12 km to 12.5 km; Fig. 6b). In winter, a dominance of anticyclones is found at the surface (0-10 m) and of cyclones just below (10-40 m, i.e. to the base of the ML), while at the very surface eddies are essentially anticyclonic year long (Fig. 6d). This dipole structure in winter results  
440 from a dominance of anticyclones at the very surface (upper 10 m) within the Canada basin year long and cyclones within the Chukchi shelf break area in winter (not shown). Below the base of the ML, the proportion between cyclones and anticyclones remains more equally distributed throughout the year, with about 55% anticyclones. Within the top 85 m, the most intense eddies are found during the stratification and de-stratification periods (stratifying and de-stratifying periods, corresponding to the onsets of sea ice growth (October and November) and to the melt season (May-July), respectively) as well as at the base.  
445 In winter, intense eddies are also found at the base of the ML in winter (Fig. 6c). Eddies persist longer in summer (7 – 8 days) than in winter when their duration lifetime is reduced by about half (Fig. 6e). Durations Lifetimes likely influence distance travelled, with eddies propagating over 15 – 16 km in summer and 7 – 8 km in winter on average (Fig. 6f). We find eddy durations to be similar to the characteristic times of spin-down through sea ice dissipation when sea ice is taken as the main drag (e.g. Meneghelli et al., 2021; Pedlosky, 1982). Yet, Lifetimes for the vast majority of eddy durations are significantly  
450 smaller eddies (85%) are significantly shorter than the theoretical mean turnaround time (85%). Thus, part of the closed and somewhat circular features that we detect detected eddies are likely not fully developed structures but rather, so belong to the "turbulent soup" that is generated in response to the surface density gradients and gets quickly dissipated by sea ice in winter. These eddy lifetimes are similar to the characteristic times of spin-down through sea ice dissipation when sea ice is taken as the main drag (e.g. < 4 days Meneghelli et al., 2021; Pedlosky, 1982). We come back to this distinction point in Sect. 4.

455

### 3.1.2 Spatial distribution of eddy characteristics

Eddy properties present large spatial variations across the surface layer of the Canadian Basin (Fig. 7). In particular, there is a strong contrast between the continental slope and the deep basin, with up to 10 times on average more individual eddies detected over the relatively small area that the slope represents larger density of eddy population over the slope ( $\approx 150$  km wide, Fig. 7a).  
460 The greater generation of eddies over the slope peaks in October, when sea ice extent is close to its minimum and winds start to increase (see Fig. ?? S9). While the production of eddies in the CB deep basin remains low on average, it becomes similar to the production over the slope when sea ice concentration drops below  $\approx 80\%$ , that is between July and November depending on the latitude (see Fig. ??a S9a). Simultaneously, eddy duration lifetime increases from evanescent ( $dt = 1 – 3$  days) below the pack in winter to about 15 days in summer on average (Fig. ??b). Yet S9b). Thus, over the domain, eddy duration shows  
465 little spatial variability (not shown). Up to 300 km off the shelf, high levels of eddy production are accompanied by intensities in the eddy field up to one order of magnitude higher than in the deep basin (Fig. 7e). This is visible all along the shelf break of the domain, that is from the Alpha-Mendeleev Ridge to Chukchi shelf break. lifetime are mainly enhanced where the ice concentration is lower than 15% (not shown).

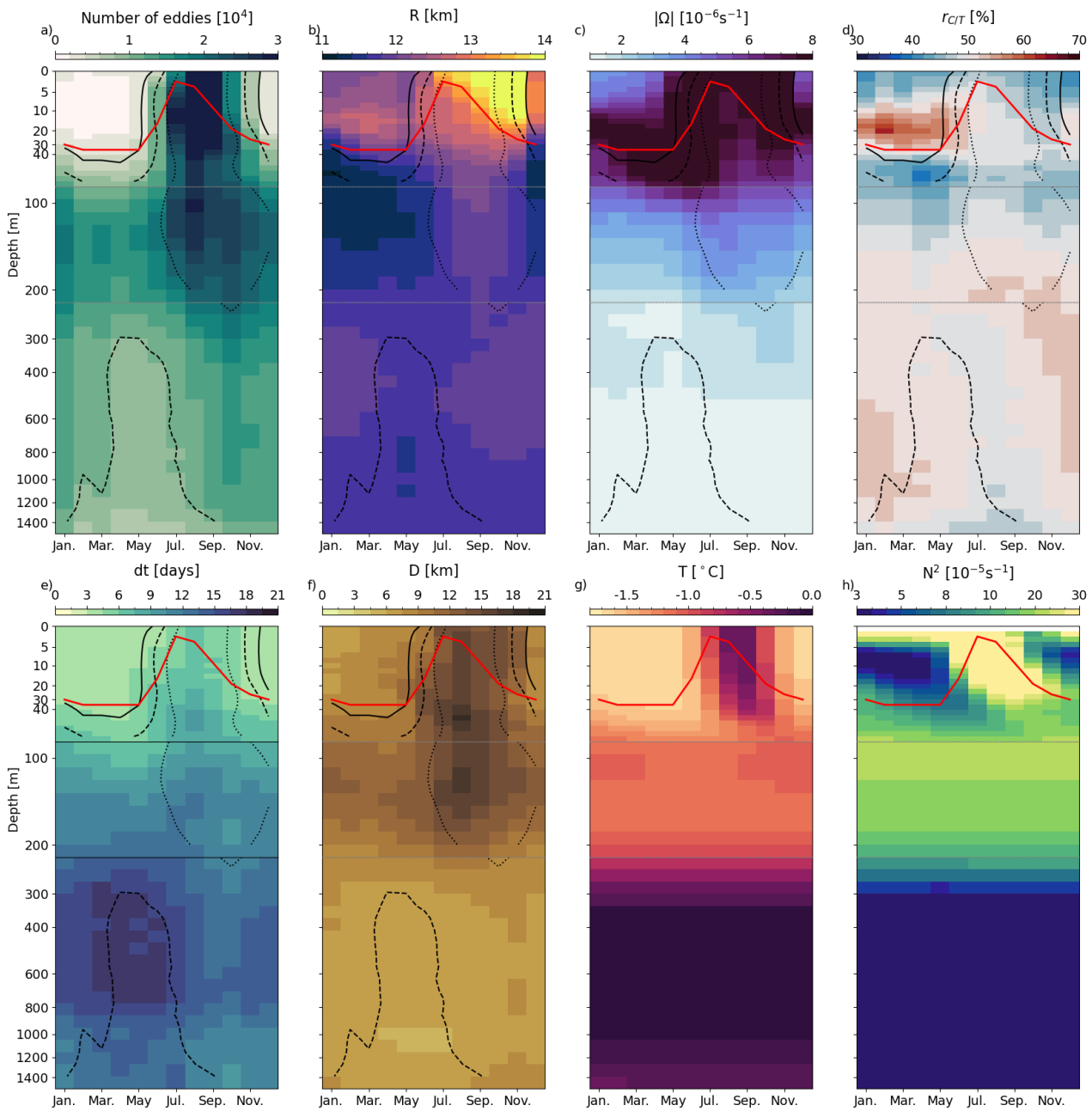


**Figure 6.** Seasonal cycle of eddy and basin properties with depth. (a) The number of eddies generated within-at each model depth level and month summed over the 26 year-years of simulation, and associated averaged properties: (b) radius, (c) intensity, (d) polarity  $r_{C/T}$  i.e. the ratio of the number of cyclones to the total number of eddies, (e) duration-lifetime, (f) distance travelled. Basin-averaged (g) potential temperature and (h) stratification ( $N^2$ ). For panels b-h, properties are averaged at each model depth level and month over the 26 years of simulation. For panels a-f, dotted, dashed and plain lines indicate the iso-contours isocontours corresponding to 5,000 10,000 and 20,000 eddies as calculated in (a), thus indicating where the statistics might be less robust due to the lower number of eddies. Note the use of a non-linear vertical axis to highlight the variability in the upper layer. Dotted horizontal grey lines delineate the three regions-layers introduced in Section 3: upper layer, pycnocline layer and Atlantic Waters layer. The red line indicates the depth of the base of the mixed layer (ML) computed from a potential density threshold referenced to 1 m of  $0.20 \text{ kg m}^{-3}$ .

Over the slope, eddies have, on average, a positive temperature anomaly ( $\approx 0.3^{\circ}\text{C}$ ) with the exception of some anomalously cold eddies forming over the Chukchi shelf. Where the mean September sea ice concentration is higher than 15%, eddies ~~have no~~ ~~do not have~~ ~~a temperature anomaly, aligning with Cassianides et al. (2023)'s detection of a majority of vortices with no significant~~ temperature anomaly. We also find a contrast in radius between the eastern and western ~~side-sides~~ of the gyre, especially off-shore the Chukchi shelf break and above ~~NWR~~ ~~Northwind ridge~~, where eddies are found to be about 60% larger (Fig. 7b). These eddies ~~have an intermediate intensity and generation rate, and are located within~~ ~~are carried within the~~ intense anticyclonic BG circulation (Fig. ??S5) and therefore travel up to 40 km throughout their ~~duration (to be contrasted with lifetime, a distance much larger than~~ the averaged distance travelled of 8 km within the CB).

Anticyclones are predominant over the centre of the gyre, while over the slope, a greater proportion of cyclones are found (Fig. 7d). ~~The investigation of vorticity~~ ~~Vorticity~~ anomalies within the CB does not indicate any preference for the generation of anticyclones (not shown). One hypothesis ~~to explain that explains~~ this cyclone/anticyclone asymmetry, ~~suggested in which~~ ~~has been formulated for~~ the Mediterranean Sea and more generally in other contexts of turbulent flows, is that anticyclones are more persistent than cyclones that tend to split ~~in~~ ~~into~~ smaller objects, leading to anticyclones being more systematically identified in ~~the datasets~~ ~~eddy censuses~~ (Stegner et al., 2021; Giulivi and Gordon, 2006). Beech et al. (2025) further suggest the role of sea ice in ~~filtering preferentially dissipating~~ small cyclones. Whether this applies to the BG is worth future investigation. ~~In particular, we suggest such mechanism is mainly visible~~ ~~We speculate that such a filtering mechanism might mainly apply~~ in the centre of the gyre where ~~mean currents are negligible and~~ the turbulent field ~~is dominant while near the edges, strong mean currents can lead to faster dissipation/destruction of eddies regardless of their polarity.~~ ~~can freely develop, while strong mean currents that generate and destroy eddies are likely to be the dominant factor in determining eddy polarity near the gyre's edges.~~

~~Up to 300 km off the shelf, high density in the eddy population is accompanied by intensities in the eddy field up to one order of magnitude higher than in the deep basin (Fig. 7c). This is visible all along the shelf break of the domain, from the Chukchi shelf break to the Canadian Arctic Archipelago shelf break.~~ The most intense eddies are found at the mouth of the McKenzie River and at Pt. Barrow (not shown), being respectively fresher and saltier than their environment (Fig. 7e,f). Along the Alaskan and Chukchi slopes, on both sides of Pt. Barrow, eddies with positive salinity anomalies are detected in the inner part of the slope, while eddies with negative anomalies are detected in the outer part. This pattern illustrates the penetration of the Pacific Waters from Pt. Barrow along the baroclinically unstable Alaskan coastal and Chukchi Slope currents (Corlett and Pickart, 2017; Spall et al., 2008) and supports ~~the~~ observations of the penetration of ~~anomalously salty eddies into the Canada Basin~~ ~~made~~ ~~eddies associated with a salty anomaly into the CB~~ at Pt. Barrow (MacKinnon et al., 2021, in the submesoscale range). ~~The elongated band of negative anomalies on the other hand~~ ~~Additionally, eddies associated with a fresh anomaly found along the outer part of the slope~~ confirm the role of fresh water input from McKenzie River in generating instabilities ~~that develop into eddies propagating downstream~~ along the anticyclonic circulation ~~producing anomalously fresh eddies downstream~~ (Kubryakov et al., 2021).

### 3.1.2 Decadal and interannual variability of eddy generation ~~Within the pycnocline layer~~

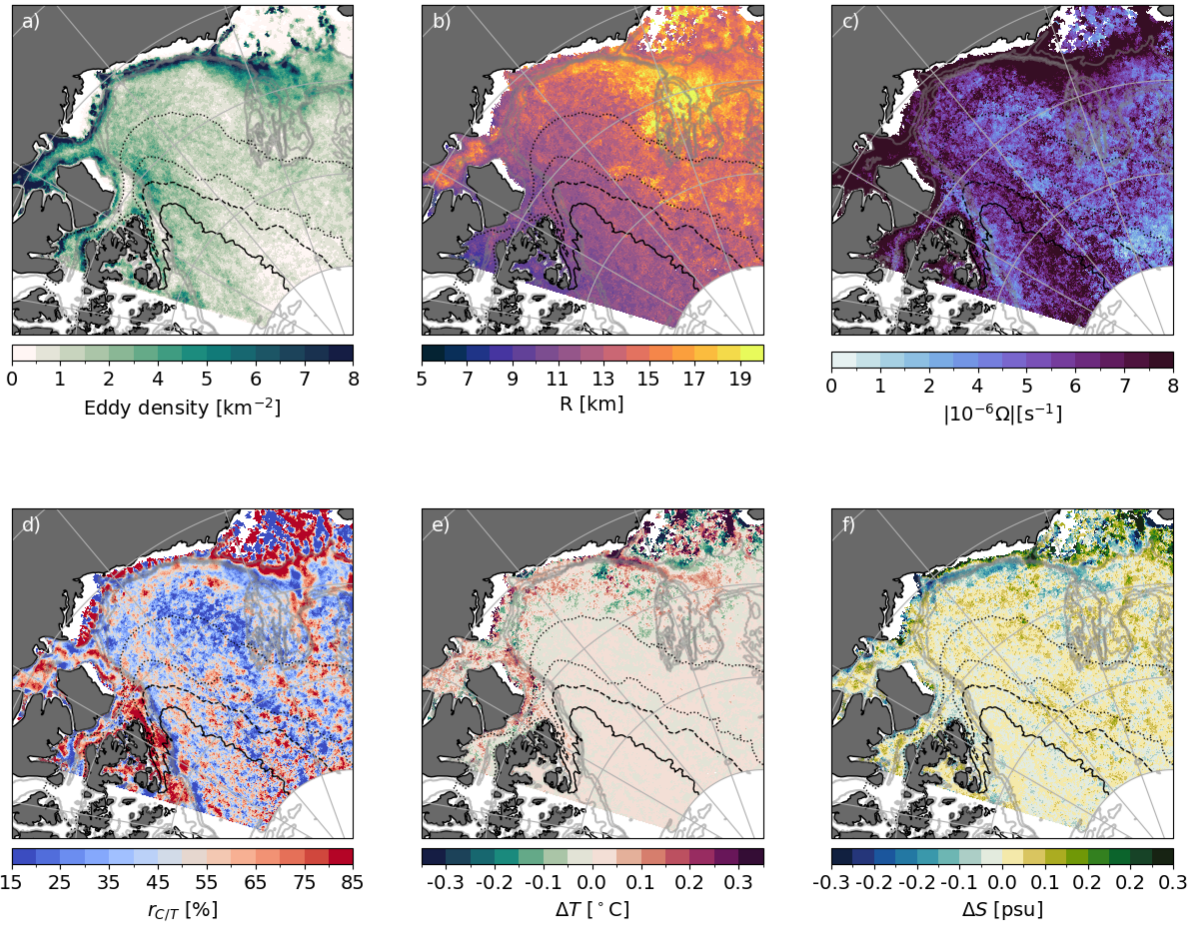


**Figure 7.** Eddy properties in the upper layer (at 30 m (i.e. within the upper layer) over the 26 years of simulation. (a) Eddy density Density of the eddy population (i.e. number of individual eddies detected per  $\text{km}^2$ ) and associated properties: (b) averaged radius, (c) intensity, (d) polarity, and anomalies of (e) temperature and (f) salinity with respect to the environment of eddies where temperatures. Temperature anomalies are taken calculated with respect to the local freezing temperature. Temperature and salinity anomalies are only accounted for when respective anomalies are significant (which represents about 15% of all eddies, see Sect. 2). All variables are extracted at nominal depth 30 m, and averaged/summed (panel a) or averaged (panels b-f) over the 26 years of simulation. Note that all fields show similar structures at all depths between 0 and 70 m except for the radii that are significantly larger within the ML (see Fig. 6c). Plain, dashed, dotted and loosely dotted black lines show respectively the 90%, 80%, 50% and 15% contours of the climatological September sea ice concentration. Gray shaded plain lines show the 100, 500, 1000, 1500 m isobaths.

Over 1995–2020, the September sea ice extent decreases by 55% in the Canadian Basin while the number of eddies generated in that region increases by 34% (comparison between the first and last 5 years of the layer-averaged number of eddies relative 505 to the 26-years average ; Fig. 10). Similar increases in the eddy number are found when looking regionally at the CB (+31%) and the Alaskan shelf area (+47%). A key difference between the two areas is that the CB is mostly energized above the mixed layer (+94% above 30 m vs -15% between 30 and 85 m). In contrast, the Alaskan shelf presents an increase in the number of eddies that is roughly constant with depth throughout the upper layer.

As sea ice shrinks, the number of eddies is expected to increase over the domain, as suggested by studies reporting on an 510 enhancement of the EKE over the Arctic. Yet, it is unclear whether the increase in the EKE is due only to the expansion of the open ocean and the MIZ, thus allowing for a higher transfer of energy from the atmosphere to the ocean, or a reduced dissipation from the sea ice (Muilwijk et al., 2024; Li et al., 2024; Rieck et al., 2025b). To investigate this question, we look 515 at the eddy density within three sea ice regions in the upper layer our domain : the pack ice (where the ice concentration is  $\geq 80\%$ ), the MIZ and the open ocean (where the ice concentration is  $\leq 15\%$ ). For a given year and sea ice region, the eddy density is defined as the total number of individual eddies detected (for that year) over the sea ice area cumulated for that year in that region. Over the 26 years, we find an increase of +10% and +20% of the eddy density in the open ocean and MIZ 520 respectively, and a slight decrease of -2% below the pack ice (Fig. ??). The small decrease of eddy density in the pack ice results from an increase above the ML of +10% and a decrease of similar amplitude below. This increase in eddy generation in the MIZ and Open Ocean points to an enhancement of eddy generation presumably through the additional energy penetrating into the ocean in line with the results of Li et al. (2024). Our results thus suggest that the number of eddies do not only increase 525 because of an expansion of the open ocean area but also because of the energy injection in all regions of the domain, although limited to the very surface the pack ice area. On interannual time scales, all the CB, Alaskan shelf areas and whole Canadian Basin show important variability in the number of eddies detected. Significant negative correlations ( $p < 0.05$ ) between the detrended number of eddies generated within the upper layer and the yearly cumulated sea ice area are found over the whole 530 domain ( $r = -0.65$ ) and more regionally over the Alaskan shelf area ( $r = -0.46$ ). Similar analyses across each depth level of the Canada basin show significant correlations at the very surface but these quickly become non-significant with depth. These results thus point to a local transfer of energy from the atmosphere to the ocean when the ice cover is diffuse enough, while it may take a greater time to penetrate at depth in regions that have a concentrated ice cover year-round like the CB.

ne series of (a) the September sea ice extent over the Canadian Basin (red, total area of the domain is  $2.7 \cdot 10^{12} \text{ km}^2$ ) and the gradient of 530 SSH averaged over the CB (similar to the maximum SSH over the gyre, not shown). (b), (c) and (d) show the layer-averaged number of individual eddies detected relative to the 26-year average within that layer for (b) the upper layer, (c) the pycnocline layer, and (d) the AW layer for the whole Canadian Basin (plain black line), the Alaskan shelf area (dashed black line) and the Canada Basin (dashed dotted line).

### 3.2 Characteristics of eddies in the pycnocline layer

#### 535 3.1.1 Mean annual and seasonal cycle of eddy characteristics

Over the 26 years of simulation, there are about ~~half~~ 30% more eddies detected ~~between the two pycnoelines in the pycnocline layer~~ ( $\sim 85\text{--}250\text{ m}$ ) than in the upper layer (~~8,900~~ 9,000 on average in the pycnocline layer) vs 6,000 eddies ~~per year per depth level on average in the upper layer per year~~; Fig. 6a). Eddies detected ~~between the two pycnoelines within the pycnocline layer~~ are evenly distributed between cyclones and anticyclones (Fig. 6d) and are found to be smaller and weaker than in the upper 540 layer on average (mean radius is decreased from  $12.4\text{ km}$  to  $11.6\text{ km}$  and intensity is decreased from  $7.4 \cdot 10^{-6}\text{ s}^{-1}$  in the upper layer to  $3.3 \cdot 10^{-6}\text{ s}^{-1}$ , Fig. 6b,c). Although weaker, eddies in the pycnocline layer last about 6 days longer than in the upper layer, likely due to the absence of ice or air drag to dissipate eddies through friction (Fig. 6e). Despite this increased longevity, the mean distance travelled by eddies in the pycnocline layer is only increased by about 1.1 km compared to the upper layer 545 (Fig. 6f), presumably because of the weaker background mean flow advecting these eddies. Therefore, of the eddies generated over the slope, only the strongest and longest-lived eddies may be able to travel far enough to reach the gyre and could thus participate in the transport of heat, salt and nutrients from the continental shelf to the deep basins (see Sect. 4).

~~Eddy characteristics in~~ In the pycnocline layer, ~~eddy characteristics~~ show a weaker seasonality compared to the upper layer. ~~This damped seasonality is expected as the upper pycnocline at  $\sim 70\text{ m}$  shields the pycnocline layer from dissipation by the sea ice.~~ Quantitatively, the ~~normalized~~ amplitude of the seasonal cycle of the number of detected eddies diminishes with depth, 550 from  $SC_N = 2.3$  at 30 m to  ~~$SC_N = 0.8$  at 85 m and~~  $SC_N = 0.5$  at 150 m (see Sect. 2 for a definition of  $SC_X$ ). The other properties also show a decreased ~~normalized~~ amplitude of their seasonal cycle compared to the upper layer, by  $\approx 60\%$  for the radius, 50% for the intensity and distance travelled, and by 40% for the ~~duration~~ ~~lifetime~~ (refer to Table 3 for detailed seasonal cycles). ~~This damped seasonality is expected as the pycnocline shields eddies from dissipation by sea ice.~~

#### 3.1.1 Spatial distribution of eddy characteristics

555 For most eddy characteristics (radius, intensity, duration, distance and polarity), the spatial distribution ~~between the two pycnoelines within the pycnocline layer~~ is generally similar to that of the upper layer (compare Fig. 7 with Fig. 8) ~~and persist year long (including the relatively high intensity along the slope). This similarity but persists throughout the year due to the absence of seasonal variability. The similarity in spatial distribution~~ with the upper layer is expected as the anticyclonic circulation that dominates most of the region investigated extends down to the ~~second pycnocline (see Fig. ??, see also ??)~~ pycnocline 560 associated to the wPW (see Fig. S5, see also Planat et al., 2025). However, the spatial distribution of the ~~eddy density in the pycnoeline layer shows a different structure than in the upper layer~~ density in eddy population is notably different between the pycnocline and the upper layers along the southern edge of the BG (Fig. 8a). There, a strong reduction in the ~~number of eddies detected~~ density of the eddy population is found compared to the shelf and deep basin (Fig. 8a). ~~This reduced eddy production~~ 565 ~~This reduced density~~ compared to the upper layer occurs despite the eddies ~~relatively strong intensity, long duration and associated distance travelled being relatively intense, long-lived and travelling relatively far along the anticyclonic flow (Fig. 8c,e,f)~~. We suggest ~~that the inner part of~~ this local reduction in eddy generation ~~to be is~~ linked to a stabilizing effect of the

continental slope. The growth of instabilities is known to be hampered over regions where the ratio of the continental slope to the isopycnal slopes is greater than 1 (Manucharyan and Isachsen, 2019), as is the case for the slope of the CB in the model (Regan et al., 2020). (not shown, see also Regan et al., 2020). However, this reduction occurs up to 250 km away from the shelfbreak. There, we observed diminished background PV gradients (not shown, see Fig. 9 from Meneghelli et al., 2021) associated to diminished baroclinic instabilities, which offer an alternative explanation for the extended area with diminished eddy density.

### 3.1.1 Decadal and interannual variability of eddy generation

Over 1995–2020, the number of individual eddies detected between the two pyenoelines shows a larger increase than in the upper layer (+45% vs +34%, Fig. 10b,e). Regionally, increases in the number of eddies are also found in the CB (+33%), and along the Alaskan coastline (+70%) as well as for short-lasting (+42%) and long-lasting (+75%) eddies (classified by comparing their turnaround time scale to their duration, see Fig. ??). The relative number of eddies generated in the pyenoeline layer shows important interannual variability, with similar variations as the upper layer, despite no significant correlations with the ice cover. In details, a strong increase in the number of eddies detected starts around the year 2000 and peaks around 2008 (+54% between 2006 and 2008, Fig. 10b,e). Concurrently, a fast accelerating period for the BG mean flow has been observed (Giles, 2012; Regan et al., 2019) and modelled (Regan et al., 2020) around 2007, and is also visible in CREG12 between 2005 and 2007 through the mean gradients of SSH averaged over the CB on Fig. 10a. The observed increase in the number of eddies that peaks in 2008 bears similarity to the EKE increase that was reported over one year by Regan et al. (2020) following the gyre acceleration in 2007. While similar interannual variability is visible in the Alaskan shelf area, the CB, however, display a strong increase in eddy generation around 2008 that persists for a couple of years beyond the peak in the BG intensity. The processes sustaining this high level of eddy generation beyond 2008 remain to be explored. The increase in the number of eddies at the end of the time period (+46% between 2012 and 2020) associated with a decrease in the gyre's intensity remains unexplained as a few more years of simulation would be necessary to conclude robustly about any trend and sustained changes.

## 590 3.2 Characteristics of eddies in the AW layer

### 3.1.1 Within the AW layer

### 3.1.2 Mean-annual and seasonal eddy characteristics

Below the second pyenoeline Below the pycnocline layer and down to 1,200 m, that is within the AW layer, the total number of eddies over the 26 years of simulation decreases by 37% compared to the pycnocline layer (from 8,900 on average 9000 per year in the pycnocline layer to 5,600–500 eddies per year per depth level, in the AW layer; Fig. 6a). This decrease is reduced to ~20% if one compares eddy density, as the area where eddies developed is reduced due to the bathymetry. Because the layer is located below the upper and lower pyenoelines, the seasonality pycnocline, the seasonal variability in eddy properties is almost

and associated properties: (b) averaged radius, (c) intensity, (d) polarity, (e) duration and (f) distance travelled. All variables are extracted at nominal depth 150 m, and averaged/summed over the 26 years of simulation. Note that all fields show similar structures at all depths between 85 and 225 m (see Fig. 6c). Plain, dashed, dotted and loosely dotted black lines show respectively the 90%, 80%, 50% and 15% contours of the climatological September sea ice concentration. Gray shaded plain lines show the 100, 500, 1000, 1500 m isobaths.

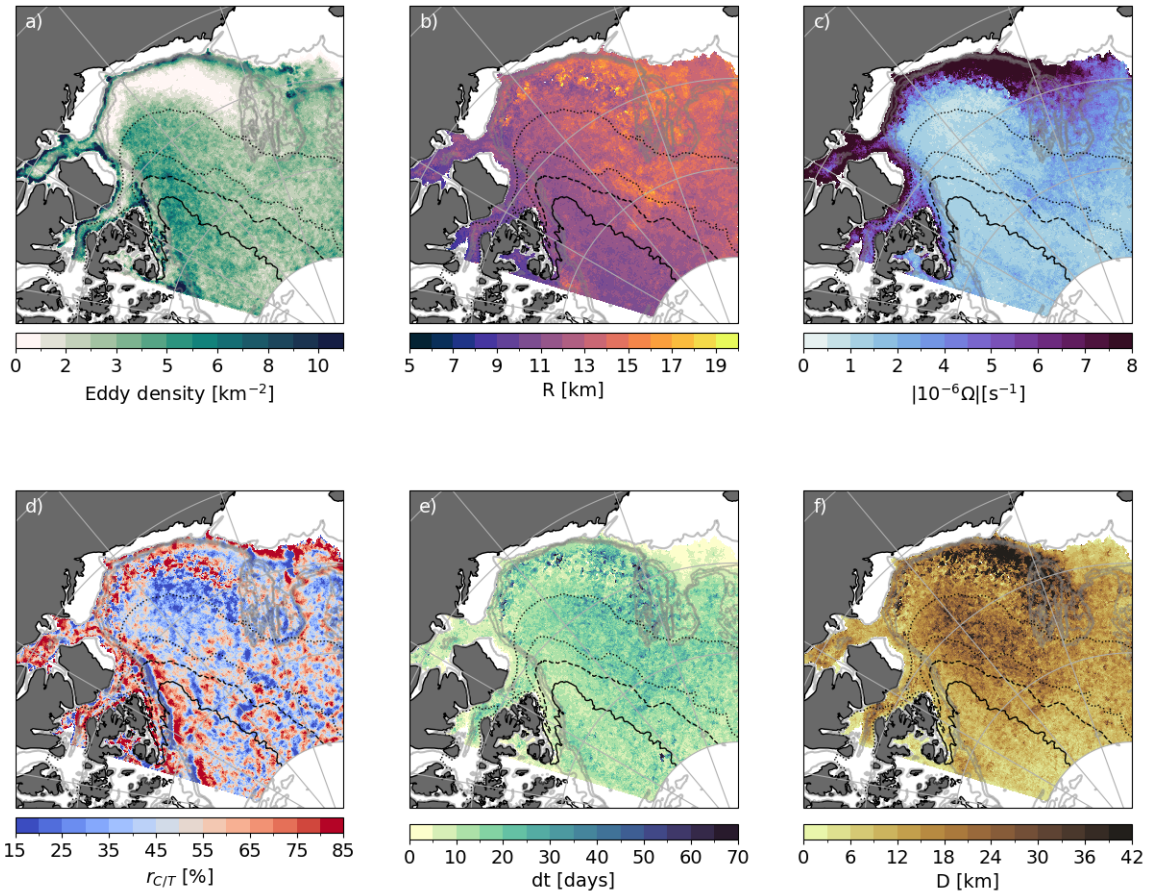


**Figure 8.** Eddy properties at 150 m (i.e. within the pycnocline layer) over the 26 years of simulation. (a) Density of the eddy population (i.e. number of individual eddies detected per  $\text{km}^2$ ) and associated properties: (b) averaged radius, (c) intensity, (d) polarity, (e) lifetime and (f) distance travelled. All variables are extracted at nominal depth 150 m, and summed (panel a) or averaged (panels b-f) over the 26 years of simulation. Note that all fields show similar structures at all depths between 85 and 225 m. Plain, dashed, dotted and loosely dotted black lines show respectively the 90%, 80%, 50% and 15% contours of the climatological September sea ice concentration. Gray lines show the 100, 500, 1000, 1500 m isobaths.

completely shut down (Fig. 6). In that layer, we find eddies ~~with similar~~ ~~similar~~ in radius ( $\approx 11.8$  km, Fig. 6b) but weaker ~~in intensity~~ than in the pycnocline layer ( $1.5 \cdot 10^{-6} \text{ s}^{-1}$  compared to  $3.3 \cdot 10^{-6} \text{ s}^{-1}$ , Fig. 6c). The distance travelled by eddies 600 decreases from 12.2 km to 7 km (Fig. 6f), and the polarity remains ~~≈ 50%~~ ~~equally shared between cyclones and anticyclones~~ (Fig. 6d). We note that the ~~average duration-averaged lifetime~~ of eddies is ~~larger~~ ~~longer~~ than in the pycnocline layer (14 days compared to 11 days) but remains small ~~considering~~ ~~despite~~ the few processes that could dissipate eddies at this depth. This 605 relatively short ~~duration-lifetime~~ may point to the fact that most of the eddies detected in this layer are not well-developed ~~according to their turnaround time~~, and hence bound to disappear quickly. Of all the eddies detected in that layer, ~~only~~ 6% ~~are well-developed so that they~~ persist for longer than their turnaround time. These ~~long-lasting~~ ~~long-lasting~~ eddies may live up to 150 days (99<sup>th</sup> percentile), which surpasses all the maximum durations detected in the other layer (~~see and matches estimates from observations of weeks to years (Hunkins, 1974; Timmermans et al., 2008). We refer the reader to~~ Sect. 4 for a discussion on ~~the~~ long-lasting eddies).

### 3.1.2 Spatial distribution of eddy characteristics

610 Within the AW layer, eddy properties show different patterns compared to the layers above. Significant differences are expected given that the mean ~~geostrophic~~ circulation of that layer departs strongly from that above (Fig. ??S5). In particular, eddies are predominantly generated over the continental slope along the path of the cyclonic boundary current carrying AW (Fig. 9a). ~~Along these~~ ~~A smaller density of eddies is generated in the rest of the domain, with some hot spots of high density in eddy population located close to the northern boundary of our domain. The latter correspond to short-lived eddies, and we discuss~~ 615 ~~more extensively the "turbulent soup" form by short-lived eddies in Sect. 4. Along the shelfbreak and boundary currents, the eddy intensity is larger by up to one order of magnitude compared to the rest of the domain (Fig. 9c). Weaker eddies are generated throughout~~ ~~Throughout~~ the rest of the domain ~~but at a smaller generation rate (4–8 eddies per km<sup>2</sup> compared to 8–12 eddies per km<sup>2</sup> along the slope). Along the~~, eddies are notably weaker. ~~No clear spatial pattern in polarity arise at the scale of the basin, except along the~~ shelf breaks of the Chukchi Sea and Canadian Archipelago, ~~polarity show anticyclones~~ 620 ~~dominating where anticyclones dominate~~ in the inshore part of the current ~~and cyclones dominating while cyclones dominate~~ in the offshore part of the current (Fig. 9d). Off the western flank of Northwind Ridge are found the largest ~~, farthest-reaching and longest-lived eddies, with averaged radii as large as (up to 20 km, travelled distances km), farthest-reaching (up to 40 km, and durations as long as km) and longest-lived (up to 60 days) eddies~~ (Fig. 9b,e,f). ~~Large uncertainties exist on the exact path of the AW in this region where AW is thought to intermittently detach from the slope-intensified cyclonic boundary current and/or form double boundary currents (McLaughlin et al., 2009; Li et al., 2020; ?; Karcher et al., 2012; Lique et al., 2015). In our model, the~~ The EKE is one order of magnitude larger in that area than within the deep basin and displays hotspots in the 625 form of large structures detaching from the cyclonic boundary current ~~hugging that hugs~~ Northwind Ridge (not shown), ~~that likely generate the large eddies detected. Finally, most hot spots in eddy density located close to the Northern boundary of our domain are associated to short-lived eddies, and the larger eddy density is likely a signature of the limitation of the detection algorithm with respect to very weak eddies that get lost over consecutive days. In this region, large uncertainties exist among the~~ literature on the exact path of the AW. The AW are thought to intermittently detach from the slope-intensified cyclonic boundary 630

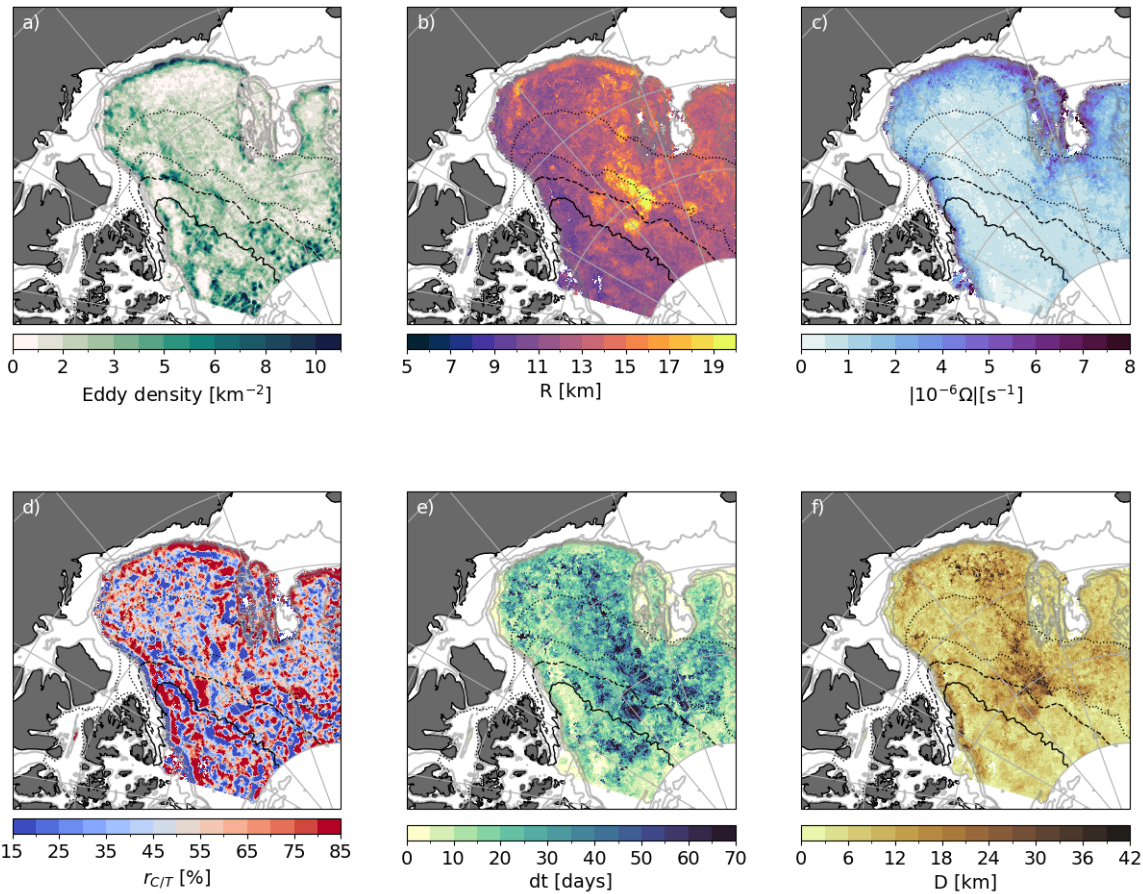


**Figure 9.** Eddy properties ~~in the AW layer~~ (at 500 m *i.e.* within the AW layer) over the 26 years of simulation. (a) ~~Eddy generation density~~ ~~Density of eddy population~~ (*i.e.* number of individual eddies detected per  $\text{km}^2$ ) and associated properties: (b) averaged radius, (c) intensity, (d) polarity, (e) duration and (f) distance travelled. All variables are extracted at nominal depth 500 m, and ~~averaged/summed~~ *panel a* or ~~averaged~~ *panels b-f* over the 26 years of simulation. Note that all fields show similar structures at all depths between 225 and 1200 m (see Fig. 6e). Plain, dashed, dotted and loosely dotted black lines show respectively the 90%, 80%, 50% and 15% contours of the climatological September sea ice concentration. Gray ~~shaded plain~~ lines show the 100, 500, 1000, 1500 m isobaths.

current, or alternatively flow along double boundary currents (McLaughlin et al., 2009; Li et al., 2020; Planat et al., 2025; Karcher et al., 2025). We suggest here some instabilities in the cyclonic boundary currents associated to the generation of large eddies.

### 3.1.2 ~~Decadal and interannual variability of eddy generation~~

635 ~~Similar to the pycnocline and surface layer, the AW layer shows a sustained increase in the number of eddies generated over the~~

### 3.2 Evolution of the population of eddies over 1995-2020

Over the last two decades, both the sea ice cover and the anticyclonic mean circulation of the Canadian Basin have drastically changed. Indeed, the sea ice extent has shrunk with a trend of  $-12.7\%$  (Meier and Stroeve, 2022), while an acceleration of the anticyclonic circulation of the BG has been found to occur around 2007 in both observations (Giles, 2012; Regan et al., 2019) and models (Regan et al., 2020) associated with a decrease in the ice cover and increased Ekman pumping, with intensified winds (Meneghelli et al., 2018b). Both this decadal change in ice cover and this fast accelerating period of the BG are represented in our model (Fig. 10a) : the sea ice extent of the Canadian Basin decreases by  $-55\%$  over the 26 years of simulation, while the mean gradients of SSH over the CB, which is a proxy for the intensity of the mean circulation at the surface, shows a step increase of  $0.15\text{mm/km}$  between 2006 and 2008, for an overall increase of  $+16\%$  (% changes are computed using averages over the first and last 5 years of the simulation). We report in the paragraphs below how the population of eddies has changed between 1995 and 2026 in light of the modifications of these two forcing fields.

Over 1995-2020, the number of eddies generated in the Canadian Basin increases in all layers, by  $+34\%$  in the upper layer,  $+45\%$  in the pycnocline layer and  $+40\%$  in the AW layer (Fig. 10d). Increases in eddy number are also found when looking regionally at the CB and the Alaskan shelf area shows an increase of  $+92\%$  while in contrast, the Canada Basin at all depths: with the exception of the AW layer that shows an overall decrease in the eddy number in the CB ( $-26\%$ ). However, the increase at the end of the time series for the CB ( $+59\%$  between 2015 and 2020) suggests a lagged increase that cannot be seen due to the length of the time series. In contrast to the layers above, little interannual variability is visible on top of the overall increase in eddy generation. This is also true for the short-lasting eddies, that represent the vast majority of the population within that layer a rebound in the eddy number is seen around 2017, thus suggesting a possible lagged increase in the eddy number in that layer. A key difference between the Alaskan Shelf and CB is that the latter is mostly energized above the mixed layer ( $+94\%$  above  $30\text{ m}$  vs  $-15\%$  between  $30$  and  $85\text{ m}$ ) while the former presents an increase in the number of eddies that is roughly constant with depth throughout the upper layer. This difference may be explained by the greater energy input in the Alaskan area that becomes seasonally ice-free earlier than the interior of the basin, where little additional energy linked to the sea ice decline can thus penetrate in the water column.

Along with the increase in the eddy population, eddies become bigger ( $+0.7\text{ km}$ ), travel further ( $+2.2\text{ km}$ ) and carry relatively warmer waters ( $+0.0027^\circ\text{C}$ ; Table. 2). These changes are in line with an increased stratification, which increases the Rossby radius. In the upper layer, eddies last longer ( $+0.6\text{ days}$ ), most probably in relation to the reduced impact of sea ice. In both the AW and pycnocline layers, but not for the long-lasting eddies, that only represent the eddy intensity is increased. This is presumably due to the fastened mean circulation, with increased MKE and EKE in all layers (not shown). Polarity remains unchanged through the 3 decades. A detailed comparison of the histograms for each property between the first and last 5 years of the simulation is offered in supplementary Fig. S10.

670 An increase in the number of eddies is expected as sea ice shrinks, and is in line with the recent literature reporting on an  
enhancement of the energy over the Arctic (Regan et al., 2020; Li et al., 2024; Manucharyan et al., 2022; Armitage et al., 2020)  
. Yet, it remains unclear whether this increase is due only to the expansion of the open ocean and the MIZ, or also to increased  
levels of energy within the MIZ and pack ice linked to the sea ice becoming less concentrated, but also thinner and more  
mobile (Kinnard et al., 2011; Kwok, 2018; Rampal et al., 2009) and to changes in atmospheric forcing, in particular. If the  
675 former applies, then the density of the eddy population within the open ocean should remain constant. To investigate this  
question, we look at the density of the eddy population within three sea ice regions in the upper layer of our domain : the  
pack ice (where the ice concentration is  $\geq 80\%$ ), the open ocean (where the ice concentration is  $\leq 15\%$ ), and the MIZ which  
lies in between. For a given year and region, the density is computed as the total number of individual eddies detected for  
that year over the mean sea ice area for that year in that region. Over the 26 years, we find an increase of +10% and +20%  
680 of the density in eddy population in the open ocean and MIZ respectively, and no change on average below the pack ice  
(Fig. S11). In the MIZ and open ocean, the increase in eddy generation is mainly a step increase in 2008 with reduced (shut  
down) interannual variability in the MIZ (Open Ocean) in the following years. This enhancement in the density of the eddy  
population presumably results from the additional energy penetrating into the ocean in the recent state of the BG, in line with  
future projections of Li et al. (2024). In the open ocean, this accumulation of energy could be attributed to the acceleration of  
685 the BG from atmospheric forcings (Giles, 2012), and in the MIZ to a combination of less compacted ice (Martin et al., 2016)  
or to the thinner ice cover (Muilwijk et al., 2024). A quantification of these different drivers is beyond the scope of this paper  
and left for future analysis. In the pack ice, the constant density results from opposing changes with an increase above the ML  
of +10% and a decrease of similar amplitude below, with strong year to year variability (see e.g. 1999 and 2008) associated  
with low sea ice concentration years.  
690 Overall, our results suggest that, in the upper layer, the number of eddies do not only increase because of an expansion of the  
open ocean area at the expense of sea ice, but also because of an energy surplus in the Canadian Basin in the MIZ and open  
ocean, in line with conclusions from other modelling studies (e.g., Rieck et al., 2025b). The increase of energy below the pack  
ice, suggested in future projections of the Arctic (Rieck et al., 2025b), is only seen in the upper mixed layer in the current  
climate.

695 On interannual time scales, the CB, Alaskan shelf area and whole Canadian Basin show important variability in the number  
of eddies detected in the upper layer. Significant correlations with the ice cover, either with the September sea ice extent, or  
with the yearly cumulated area with ice less concentrated than 80%, are only visible at the surface (down to  $\approx 20$  m, that is  
approximately down to the basis of the mixed layer), at the exception of the Alaskan area where they are found significant  
700 deeper (not shown).

In both the upper and pycnocline layers, the number of eddies starts rising around 2000 before culminating in 2008 (+54%  
between 2006 and 2008 in the pycnocline layer, Fig. 10b,c). The increase in the number of eddies that peaks in 2008 in our  
model bears similarity to the EKE increase that was reported by Regan et al. (2020) to occur over one year following the gyre  
acceleration in 2007. The authors suggest that beyond 2007-2008, the BG is able to expand spatially over NorthWind Ridge and

	$R$ [km]	$D$ [km]	$dt$ [days]	$ \Omega $ [ $10^{-7} \text{s}^{-1}$ ]	$\Delta S$	$\Delta T$	$r_{CT}$ [%]
Upper layer (0 - 85 m)	1 ; 8%	2.4 ; 21%	0.6 ; 10%	-2.1 ; -3%	-0.008	0.004	-0.7
Pycnocline layer (85 - 225 m)	0.5 ; 4%	2.0 ; 18%	-1.3 ; -11%	7.9 ; 26%	0.003 ;	0.004 ;	-0.06
AW layer (225 - 1200 m)	0.4 ; 4%	2.0 ; 30%	-1.4 ; -9%	7.4 ; 57%	-2.5e-5	0.0009	3
All (0-1200 m)	0.7 ; 6%	2.2 ; 22 %	-0.5 ; -5%	3 ; 7 %	0.0003	0.0027	0.8

**Table 2.** Change in mean eddy properties for each layer when comparing the last 5 years of the simulation and first 5 years. Red indicate an increase, blue a decrease. Also reported are relative increases in % for the mean radius, distance, duration and intensity.

705 thus the need for eddies to release the accumulated potential energy is reduced. The transient increase in the number of eddies reported in our analysis thus tends to confirm this hypothesis, with a slightly longer equilibration time. In the pycnocline layer of the CB, the increase in the eddy number in 2008 persists for an additional couple of years in contrast to the Alaskan shelf area and basin average where the increase remains punctual. Further down, the AW layer also displays an increase, yet weaker, in the number of eddies in the CB (Fig. 10d). This increase at depth suggests a direct top-down coupling between the BG and the 710 AW layers, despite the insulation of the pycnocline, as documented by Lique and Johnson (2015) and Lique et al. (2015) for the mean circulation of the AW layer. The processes sustaining the increase in the number of eddies within both the pycnocline and AW layer for the 5 years following the increase of the BG remain to be explored. Additionally, we note that the number of eddies generally keeps increasing after 2016, while the gyre intensity declines. Our simulation lacks a few more years to interpret changes.

715 Within the AW layer, little interannual variability in the number of eddies is found in contrast to the layers above (Fig. 10d). However, when looking at the long-lasting eddies (6% of the total population and display), we do see important year-to-year variability (see Fig. S12). These more persistent features show a large relative increase (+300%) starting around 2011 (see Fig. ??). This is mostly, which is mostly due to an increase in the number of large eddies located east of NWR that are possibly associated with the cyclonic boundary current detaching from the bathymetry. These large structures occur Northwind Ridge. 720 These structures, which are large (30-50 km), develop in particular in the late years of the simulation (2012-2020) when the cyclonic flow on the north-western boundary current on the Northwest flank of Northwind Ridge reverses to an anticyclonic flow with increased horizontal shear (not shown). What drives these changes in the AW mean and eddy circulations and how they pathways, and how the latter influence the generation of large eddies is beyond the scope of this paper and is left for future analysis. The number of eddies in the Canada Basin also exhibits some interannual variability, in particular showing a small but significant transient increase around 2007-2010 similar to the one described in the pycnocline layer associated with the acceleration of the Gyre. Such a direct top-down coupling between the Beaufort Gyre and the AW circulation was already documented by Lique and Johnson (2015); Lique et al. (2015) for the mean circulation of the AW layer. This more energetic mean flow may in turns generates more mesoscale eddies.

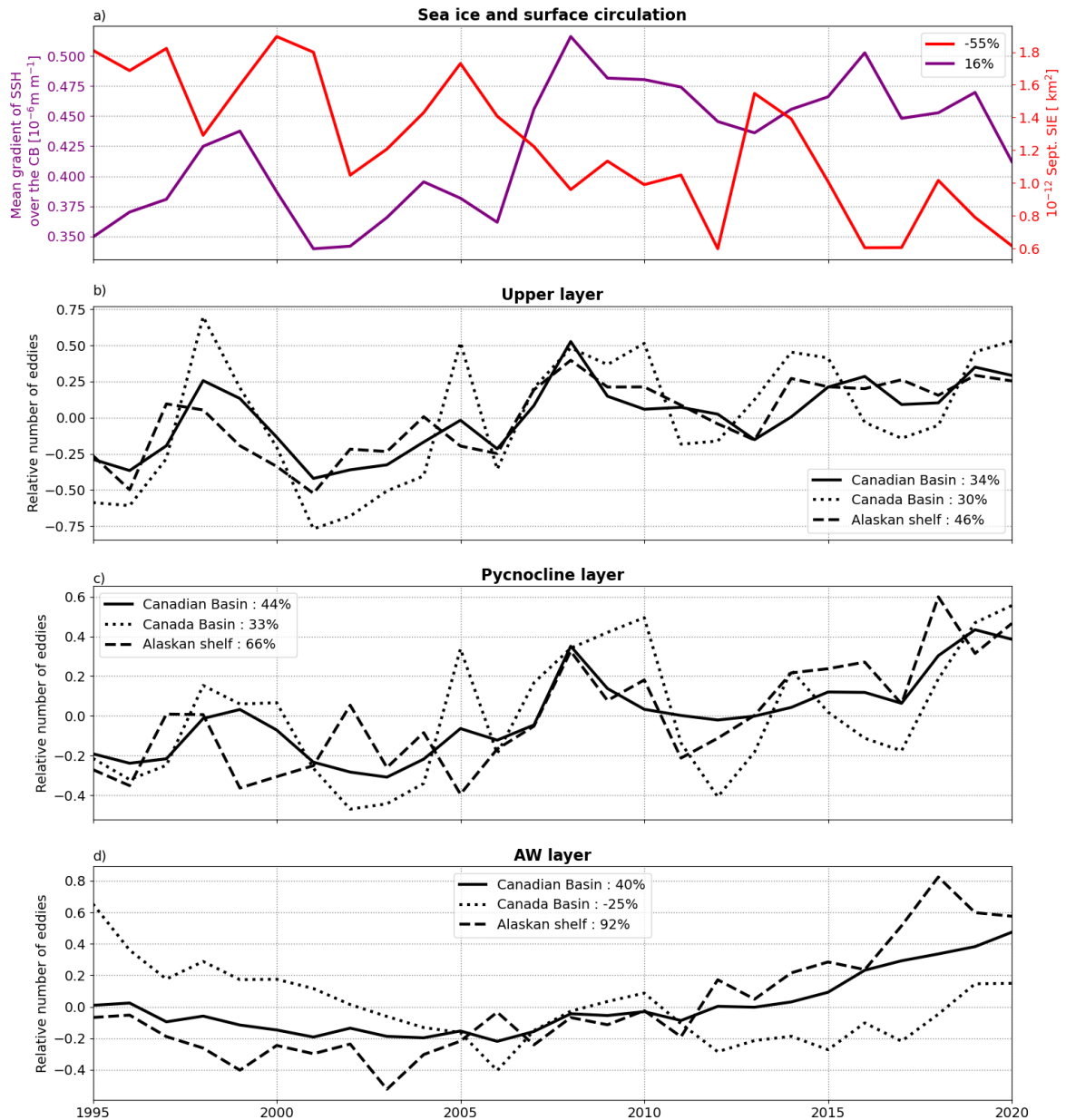


**Figure 10.** Time series of (a) the September sea ice extent over the Canadian Basin (red, total area of the domain is  $2.7 \cdot 10^{12} \text{ km}^2$ ) and norm of the gradient of SSH calculated at every location of the domain and averaged over the CB. (b), (c) and (d) show the layered-averaged number of eddies relative to the 26-year average for (b) the upper layer, (c) the pycnocline layer, and (d) the AW layer, further divided into the whole Canadian Basin (plain black line), the Alaskan shelf area (dashed black line) and the Canada Basin (dashed dotted line). Reporting numbers of eddies relative to the 1995–2020 average for each depth level permits a comparison of the temporal evolution of depth levels with different absolute numbers of eddies.

#### 4 Discussion and conclusion

730 In this study, we apply an eddy detection and tracking algorithm to the output of a high-resolution regional model of the Arctic, in order to document the characteristics of mesoscale eddies in the Canadian Basin. ~~We and examine the evolution in the number and characteristics of eddies over 1995-2020. Over that period, we report an average of 6,250 ≈ 6,000 eddies generated per year and per model depth within the top 1,200 m in the surface layer, ≈ 9,000 eddies in the pycnocline layer, and ≈ 5,500 in the AW layer of the Canadian Basin for the period 1995-2020.~~ Most of these eddies are found to be the size of 735 the Rossby radius of deformation (mean eddy radius ~~of~~ about 12.1 km), stationary (distance travelled ~~of~~ about 11.1 km) and short lasting (~~duration lifetime of~~ about 10 days; Fig. 4). The distribution between cyclones and anticyclones is about equal in the investigated domain. In addition, ~~most the majority of~~ eddies do not have a temperature nor salinity anomaly relative to their environment, ~~although some significant anomalies are visible along the shelf in the surface layer (Fig. 7e,f).~~ All the 740 documented properties (radius, polarity, intensity, ~~duration lifetime~~, distance travelled and temperature and salinity anomaly) vary significantly across space and time (see Table 3), ~~thus suggesting a variety of processes that generate and dissipate pointing to the role of the environment, such as the stratification, sea ice or main currents, in setting different processes important for the generation and dissipation of~~ eddies in the ~~stratified~~ Canadian basin.

Our analysis highlights three layers ~~within the Canadian Basin with consistent characteristics that arise from the stratification of the Canadian Basin and show consistent characteristics for eddies~~ across the vertical. ~~It is important to note that the definition of the three layers relies on the statistical properties of the whole eddy field over 26 years and hence does not account for temporal variability of the mean circulation, the location of the gyre, and the mean isopycnal depths and slopes. Thus, the depths used as delimiters of the three layers do not necessarily correspond to the actual, instantaneous pycnoclines that they are assumed to represent at all times. This is particularly true where the isopycnal surfaces are strongly tilted or even outcrop over the slope and the shelf break. There, fixed depth layers ensure that there is no averaging done between regions in contact with sea ice and those away from the sea ice influence that would otherwise complicate the interpretation of the results. The results presented in this study, and in particular the spatial structure of the eddy properties and their temporal variability, remain consistent when slightly varying the layers' upper and lower boundaries indicating the robustness of the key features reported for the three layers especially in the centre of the BG where the isopycnals are relatively flat.~~

750 In the upper layer (top 85 m), which lies ~~above the first pycnocline on average on average above the pycnocline~~, eddy properties display a significant seasonal cycle generally in phase with that of sea ice. ~~The largest generation rate for eddies occurs Eddy population is the densest~~ when sea ice concentration decreases below 80%, a threshold in line with the results of Manucharyan and Thompson (2022), ~~and over the continental slope~~. At about ~70 m, the ~~first~~ pycnocline insulates the eddy field from dissipation by sea ice. Therefore, weaker seasonality is detected in the eddy characteristics below this depth. ~~However, interannual variability in the number of eddies related to changes in the large scale circulation can still be observed. Over 2007-2008, the BG acceleration likely leads to an increase in the number of eddies followed by a quick return to the pre-acceleration number in 2009, as suggested by Regan et al. (2020). An increase in number of eddies can be detected down to 1200 m in the CB, though it takes about 4 years to drop to pre-acceleration levels of eddy generation after 2008. The reasons of this slower decrease~~

remains unexplained and deserves further investigation in future work. Apart for this transient increase in number of eddies in the CB, the AW layer show Between 85 m and 225 m depth, a reduced density in the eddy population is found within a 250 km wide area along the Alaskan shelf break that is attributed to the smaller gradients of background potential vorticity. Deeper down, the AW layer shows a muted seasonal cycle in eddy properties and little to no similarities to the layers above, in line with due to the efficient insulation of the lower this region by the pycnocline. In particular, while the upper and pycnocline layers of the Canadian Basin show anticyclones forming preferably at the centre of the Beaufort Gyre, in the AW layer anticyclones are found, a symmetry is found along the slope, with anticyclones forming in-shore and cyclones off-shore of the boundary current along the slope. Finally, it is important to note that the definition of the three layers relies on the statistical properties of the whole eddy field over 26 years and does not account for temporal variability of.

The 1995-2020 period is marked by an overall rise in eddy density at all depths (+35 – 45%), in line with predictions of an increasingly energetic Arctic Ocean (Rieck et al., 2025b; Li et al., 2024) with reduced ice cover (Meredith et al., 2001; Meier and Stroeve, 2007). A smaller increase is visible in the upper open ocean and upper MIZ (+10%), and limited to the mean circulation, mixed layer of the pack ice area. We argue that the higher density in the eddy population is the result of an increasing penetration of energy in the upper layers of the basin where the ice concentration is small enough. Therefore, in the MIZ and open ocean, these results confirm findings from Rieck et al. (2025b) of an increased energy input associated to more energy conversion toward EKE, and from Li et al. (2024) who associate this increased EKE to higher baroclinic instabilities, despite increased eddy killing with more mobile ice, in simulations of the future Arctic. Large interannual variability in the number of eddies is visible in the upper and pycnocline layers, with in particular a peak in the eddy population between 2007-2009, when the BG is known to have accelerated. Post 2010, the eddy population is similar in the upper and pycnocline layer to that prior to 2007, which tend to confirm Regan et al. (2020) hypothesis that the gyre is able to expand above Northwind Ridge and thus diminish the baroclinic instabilities. We however report longer equilibration time for the number of eddies, especially in the location of the gyre, and CB. The upper layer additionally shows the imprint of the ice cover on yearly time scale with significant correlations between the ice area and the mean isopyenal depths and slopes which additionally vary across the basin. Thus, the depths used as delimiters of the three layers do not necessarily correspond to the actual, instantaneous pycnoclines that they are assumed to represent at all times. Nevertheless, the results presented in this study, and in particular the spatial structure of the eddy properties and their temporal variability, remain consistent when slightly varying the layers' upper and lower boundaries indicating the robustness of the key features reported for the three layers, number of eddies along the Alaskan shelf break and at the very surface of the CB. Overall, the interannual and decadal variability of the pycnocline and surface layers result from both local changes in sea ice dissipation and large scale changes in energy input.

Of particular interest when comparing to our 50-50 ratio of cyclones and anticyclones is the ratio of 95% anticyclones exhibited by the ITP dataset (Cassianides et al., 2023; Zhao et al., 2014), although one should keep in mind that this dataset contains primarily sub-mesoscale features. Even more surprising, the symmetry remains valid if we subsample the dataset to only account for small eddies ( $R < 15$  km) that are more likely to resemble the submesoscale coherent vortices detected from the ITP dataset. The predominance of anticyclones exhibited by the ITP dataset concerns the centre of the BG which is where

	Nmb. of eddies	$R$ [km]		$dt$ [days]		$D$ [km]		$r_{C/T}$ [%]	$ \Omega $ [ $\text{s}^{-1}$ ]	$\Delta T$ [ $^{\circ}\text{C}$ ]						
Upper layer (0 - 85 m)	6000	2.4	12.4	0.1	5.4	0.6	11.3	0.7	48.1	0.09	$7.410^{-6}$	0.4	0.08	1.7	-0.0	
Pycnocline layer (85 - 225 m)	8900	9000	0.6	11.6	0.04	10.8	0.1	12.2	0.3	49.5	0.05	$3.310^{-6}$	0.3	0.01	5.1	0.0
AW layer (225 - 1200 m)	5600	5500	0.5	11.8	0.02	14.2	0.3	7.1	0.1	50.8	0.06	$1.510^{-6}$	0.2	0.003	1.1	-0.0
<b>Total</b>	<b>6250</b>	<b>6000</b>	2.6	12.1	0.06	9.9	0.2	11.1	0.4	49	0.05	$4.610^{-6}$	0.04	0.04	1.6	-0.0

**Table 3.** Mean (left) and seasonal cycle amplitudes (right) of the eddy properties reported along this manuscript for each layer and for the Canadian Basin as a whole.

ITPs are mainly deployed due to the sea ice being the thickest (see App. ?? for details). A vertical asymmetry with the formation of dipoles of cyclones at the surface and anticyclones subducting within the pycnocline was suggested to explain the asymmetry 800 observed in the ITP dataset (Manucharyan and Timmermans, 2013). A similar asymmetry was suggested in the Southern Ocean to explain the predominance of cyclones observed at the surface in the MIZ (Auger et al., 2023). In our model, One of the centre of striking and most intriguing characteristic of the BG does display eddy field reported so far in the literature is the eddy 805 polarity, ranging from  $r_{C/A} = 5\%$  to  $r_{C/A} = 70\%$  (see Sect. 1 Cassianides et al., 2023; Kozlov et al., 2019). At the scale of the Canadian Basin, as many anticyclones as cyclones are found in the upper and pycnocline layers of our model. This partition 810 is maintained for small eddies ( $< 15$  km), or long-lived eddies (not shown). Yet, the polarity of eddies shows a marked spatial pattern over the Canadian Basin with a larger proportion of anticyclones than cyclones ( $\approx 70\%$  anticyclones) in the centre of the BG (see Figures 7d, and 8d) but no evidence of such vertical structure appears. More specifically, This predominance 815 of anticyclones aligns with that estimated using dataset based on ITPs (Cassianides et al., 2023; Zhao et al., 2014), though observations suggest a much higher proportion of anticyclones in that region (95% versus 65% in our model when applying our eddy detection following the temporal and spatial sampling of the ITPs, we find a proportion of anticyclones that increases 820 on average from 51% to 65% in our model. Though the comparison with see Fig. S13). Although the comparison between the ITP dataset and our model is somewhat limited by the fact that the observed eddy field may be dominated by sub-mesoscale features, which our model does not resolve, our results suggest that part of the anticyclonic dominance documented by the ITP dataset is simply linked to the ITP sampling location, as was already suggested by Beech et al. (2025). Due to the limits of both 825 the detection algorithm and the model's ability to resolve the smaller Rossby radius and associated mesoscale instabilities over the shelf, we cannot extend this analysis to the satellite sampling area that mostly covers Northwind Ridge and the Chukchi shelf (see Figure 2 from Kozlov et al., 2019). Still, we do observe a higher ratio of cyclones along the edges of the gyre (Figure 7d) and suggest it could correspond to the dominance of cyclones over anticyclones documented in Kozlov et al. (2019). Yet, 830 a proper and detailed comparison with observations would require using a model at higher-resolution given that most features identified with moorings, ITPs or satellite fall between the meso- and the submeso-scales. Such a comparison would also benefit from an adequate model subsampling, through an Observing System Simulation Experiments, to take into account the 835 observations sampling biases.

Our algorithm identifies as "eddy" a broad range of features, from the ephemeral ones that last a couple of days to the more persistent ones that are likely more coherent. When separating between short and long-lasting eddies based on their duration

825 being respectively shorter or longer than their turnaround time, we find that the bulk of the eddy dataset consists of short-lasting eddies. ~~The which we refer to as a "turbulent soup". Within this ephemeral eddy population that our study detects is likely not represented in observational dataset, it is likely that some short features are artefact of the tracking algorithm, that may lose track of the weakest eddies, or of eddies splitting/merging. The OW detection algorithm is known to be biased towards weak eddies. Yet, most of the features are likely actual, short-lasting eddies that are evanescent by nature. Within the upper layer, the very~~  
830 ~~short lifetime of these eddies could be attributed to the presence of sea ice (spindown time scale of eddies due to ice friction is estimated around 10-20 days). At depth, weak vortices have been suggested to form from the stirring of interior PV gradients (Manucharyan and Stewart, 2022)~~  
~~Overall, these relatively weak and short-lasting eddies that form a turbulent soup are not captured by observational dataset, which may explain some of the important differences found with the literature based on observations. Yet between our census and the observation-based literature. Nonetheless, these eddies may play an important role in the transfer of energy, and we leave for future analysis to quantify their integrated role in the penetration of heat, salt and nutrients into the deep basin.~~  
835

Long-lasting eddies may resemble more the eddy population captured by observations. We find that these eddies represent 15% of the population in the upper layer, 10% in the pycnocline layer and 6% in the AW layer (see also the mean statistical properties of long-lasting eddies in [Appendix ??](#) [supplementary Fig. S14](#)). A fraction of these eddies display temperature anomalies, in particular along the shelf break, ~~while little salinity anomaly is observed within this eddy subset~~. These anomalies 840 are mostly positive at the surface where ~~they~~ [eddies](#) are formed either within the mixed layer or the warm Near Surface Temperature Maximum; and in the upper part of the pycnocline layer, where they form within the warm summer Pacific Waters [\(not shown\)](#). In contrast, these anomalies are mostly negative in the lower part of the pycnocline layer where they form in the cold winter Pacific Waters [\(not shown\)](#). Note that because these long-lasting eddies are mostly generated in regions of ~~intense eddy generation~~ [high density in eddy population](#), such as Pt. Barrow, ~~the environment surrounding these eddies has~~ 845 ~~strong temperature gradients and thus the anomalies do not meet the "significant" criteria—despite the anomaly being clearly visible~~ [it is difficult to quantify the associated anomaly in temperature and salinity. Still, a visual inspection seems to support the presence of strong anomalies at Pt. Barrow](#) (see Fig. 11). ~~Still, because~~ [Because](#) these long-lasting eddies travel for a few tens of kilometres, we hypothesize that the most coherent eddies actively play a role in transporting heat, in line with previous observations of warm eddies directly penetrating into the CB from Point Barrow (MacKinnon et al., 2021). One example of 850 such an eddy is given on Fig. 11a, with an anticyclone carrying warm water off-shore when leaving Pt Barrow. This eddy is seen to subduct at depth from mi-September, with a colder and fresher layer developing above (Fig. 11b). However, a robust quantification of the heat transport associated with these eddies is not trivial as it requires computing the temperature anomaly which is highly dependent upon the definition of the environment. This analysis is thus left for future work.

855 To conclude, we present a first characterization of the spatio-temporal properties of mesoscale eddies in the Canadian Basin. By doing so, we [unraveled](#) [reveal](#) strong differences in eddy properties across ~~the basin and seasons~~ [space and time](#), as well as important variability in the number of eddies generated over 1995-2020. ~~By providing a thorough characterization of eddy properties in the Canada Basin, this model-based eddy census can inform the analyses and interpretation of eddy censuses based on observations and help quantify some of the biases associated to in-situ deployments. Furthermore, our dataset in relation to~~

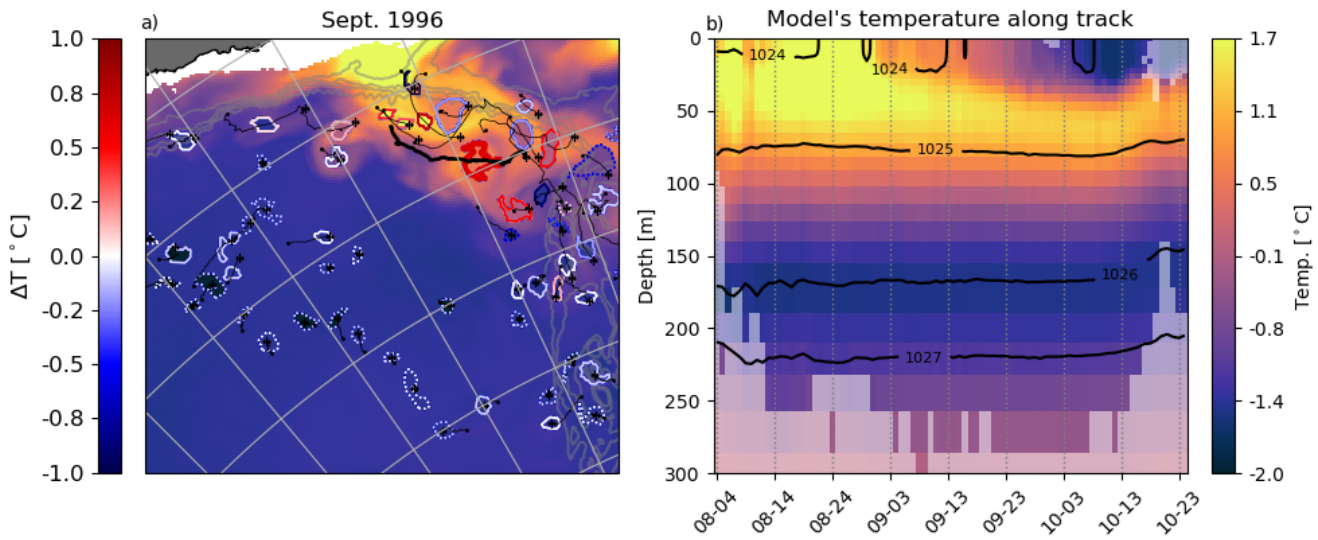


**Figure 11.** (a) Conservative Temperature at 30 m in September 1996 overlaid with contours corresponding to all long-lasting eddies detected (and not necessarily born for the first time) on September 16th 1996. Coloured Colors of contours indicate the temperature anomaly of eddies, and thin black lines their trajectory. Eddies are colored coloured (filled) by their mean temperature. (b) Model Conservative temperature along the eddy track identified on (a) with a thicker black line. At a given depth, intense color shading indicates that the algorithm detects an eddy at that depth, location and time while pale color shading indicates that no eddy is detected. Thick black lines show isopycnals along the eddy track.

860 ~~the loss of sea ice and acceleration of the BG. Our eddy census can thus provide a benchmark against which censuses from other models could be compared, and~~ could form a starting point to explore questions that remain on the BG dynamical and thermodynamical equilibrium, as well as on the transport and ~~stirring-mixing~~ of nutrients, salt, or other tracers. ~~In particular, future work could include an analysis of the interannual-to-decadal evolution of the eddy properties to help investigate their possible future effects on the environment through transport and stirring of nutrients, salt, or other tracers as sea ice retreats and the BG gets more energetic.~~

865 *Code and data availability.* The *eddytools* python package used to perform the eddy detection and tracking along with its documentation is available at <https://github.com/jk-rieck/eddytools@N-tracking-properties>. The scripts used in this study to detect, track and analyse the mesoscale eddies are available at [https://github.com/noemieplanat/Eddies\\_CB/releases/tag/submission](https://github.com/noemieplanat/Eddies_CB/releases/tag/submission). The documentation of the CREG12 experiment can be found in Talandier and Lique (2024). The detection and tracking for 30, 69, 147 and 508 m depth are available here 870 xxx. Fresh water content estimates were obtained from <https://www2.whoi.edu/site/beaufortgyre/data/freshwater-content-gridded-data/>, accessed on October 1st, 2025. The World Ocean Atlas (WOA) 2023 climatology was downloaded from <https://www.ncei.noaa.gov/access/world-ocean-atlas-2023/>, accessed in January 2025 (Locarnini et al., 2024; Reagan et al., 2024). Arctic dynamic topography/geostrophic currents data were provided by the Centre for Polar Observation and Modelling, University College London (Armitage et al., 2016, 2017). Sea ice concentration were obtained from the National Snow and Ice Data Center (NSIDC, DiGirolamo et al., 2022). PIOMAS Reanalysis 875 (Zhang and Rothrock, 2003) was downloaded from <https://psc.apl.uw.edu/research/projects/arctic-sea-ice-volume-anomaly/>

*Author contributions.* NP designed and conducted the study with input from COD, CL and LBT. CT and CL ran CREG12 model. JKR built the eddytools python package and NP applied it on the output of CREG12 with appropriate modifications. NP processed and analyzed the eddy database. NP, JKR, COD, CL and LBT contributed to the interpretation. NP wrote the manuscript, with contribution from COD, CL, LBT, JKR and CT for editing.

880 *Competing interests.* The authors declare no conflict of interest.

*Acknowledgements.* NP was supported by the Fonds de recherche du Québec - Nature et Technologie (FRQNT) through a Doctoral Training Scholarship, a Natural Sciences and Engineering Research Council of Canada (NSERC) Accelerator Supplements awarded to COD (grant no. RGPAS/2018-522502), and a NSERC Discovery Grant awarded to BT (grant no. RGPIN/2018-04838). NP also received a scholarship from ISblue (Interdisciplinary graduate school for the blue planet - ANR-17-EURE-0015) and financial support from Québec-Océan for 885 this work. COD and JKR acknowledge funding from NSERC through the Accelerator Supplements (grant no. RGPAS/2018-522502) and a Canada Research Chair (grant no. 252794), both awarded to COD. NP, COD, CL, JKR and LBT acknowledge the financial support from the Fonds de recherche du Québec – Nature et technologies (FRQNT) and the French Ministry of Europe and Foreign Affairs through the Samuel-de-Champlain grant (<https://doi.org/10.69777/329860>). CL and CT were supported by funding from the CLIMArcTIC project funded by the

“PPR Océan et Climat—France 2030” (contract ANR-22-POCE-0005). The pan-Arctic simulations were performed using HPC resources  
890 from the French GENCI-CINES center (Grant 2023-A0130107420). The authors also acknowledge the technical and scientific contributions  
of Benjamin Valette and Sacha Coez to the preparatory phase of the study.

## 5 Mean Kinetic Energy from CREG12 and from mooring estimates of von Appen et al. (2022)

Energy (MKE) computed from monthly averages and averaged over the 26 years of simulation (a) within the surface layer at 30 m, (b)  
895 within the halocline at 69 m and (c) within the AW layer at 508 m. Super-imposed on (b) are mooring estimates of MKE  
from von Appen et al. (2022) computed for depths between 50–100 m, corresponding to monthly deviations, please refer to  
this paper for exact calculation methodology.

## 5 Sensitivity to method's parameters $\alpha$

ty (dotted lines) and number of eddies detected (plain lines); median and 90/10-th percentiles for (b) the radius, (c) the intensity (absolute  
value of vorticity  $\Omega$ ) and (d) the duration when varying the detection parameter  $\alpha$  from 0.2 to 0.5. Sensibility is assessed at 35  
900 m, 69 m, 120 m, 200 m and 550 m for one year (chosen randomly as 2001) and for the whole Canadian Basin.

## 5 Changes of eddy properties simultaneously along 2 properties

istogram of duration, intensity and radius simultaneously at 30 m (first column), 150 m (second column) and 500 m (last column). First  
row display duration vs radius, second row duration vs intensity and last row radius vs intensity. Plain, dashed, loosely dashed,  
very loosely dashed and dotted lines indicate iso-contours of 10, 50, 100, 500 and 1000 eddies.

## 905 5 Seasonal changes comparatively along the coast and off shore

ovmöller diagram of a latitudinal section from the Alaskan shelf to the center of the Arctic (see red line on Fig. 1) against seasons for (a)  
the total number of eddies detected over the 26 years and (b) eddy duration. Both fields are summed or averaged zonally across  
a band of 150 km and vertically averaged within the upper layer (from surface to 85 m). Black plain, dashed and dotted lines  
910 indicate the 0.15, 0.5 and 0.8 sea ice fraction. Orange plain, dashed and dotted lines indicate the 5 m, 20 m and 40 m mixed  
layer depth.

## 5 Long-eddies characteristics

Same as Fig. 4 for long-lived eddies only

Time series of the relative number of eddies generated within the Canadian Basin for (a) the upper layer, (b) the pycnocline layer and (c) the AW layer, for respectively the short eddies (dashed lines), long eddies (dotted lines) and for all eddies (plain lines, identical to Fig. 10).  
915

## 5 Spatial repartition of ITPs across the CB between 2003 and 2024

We compute an occupation ratio for the ITP dataset on an Equal-Area Scalable Earth grid of 25 km large. We include all ITPs processed to level-3 of post-processing between 2003 and 2024 (Toole et al., 2011) and the profiles are binned per day. The occupation is computed for each grid cell, as the number of profiles by the total number of profiles (Fig. ??). Number of ITP profiles available per Equal-Area Scalable Earth grid cell for an EASE grid of 25 km large. All ITPs processed to level-3 of post-processing between 2003 and 2024 are included and binned per day (Toole et al., 2011).  
920

## 5 Time series of eddy generation for the different sea ice concentration (sic) categories: Open Ocean ( $\text{sic} < 0.15\%$ ), MIZ ( $0.15\% < \text{sic} < 0.8\%$ ) and Pack ice ( $\text{sic} > 0.8\%$ )

Time series of the relative number of eddies generated within the Canadian Basin in the upper layer for the three sea ice regions : Open Ocean (dashed lines), MIZ (dash-dotted lines) and Pack ice (dotted lines). The time series are weighted (b, respectively not weighted on panel a) by the yearly cumulated ice area of each region.  
925

## References

Antonov, J. I., Seidov, D., Boyer, T. P., Locarnini, R. A., Mishonov, A. V., Garcia, H. E., Baranova, O. K., Zweng, M. M., and Johnson, D. R.: World Ocean Atlas 2009, Volume 2: Salinity., Tech. rep., U.S. Government Printing Office, Washington, D.C., 2010.

930 Armitage, T. W. K., Bacon, S., Ridout, A. L., Thomas, S. F., Aksenov, Y., and Wingham, D. J.: Arctic sea surface height variability and change from satellite radar altimetry and GRACE, 2003–2014, *Journal of Geophysical Research*, [Dataset][http://www.cpom.ucl.ac.uk/dynamic\\_topography/](http://www.cpom.ucl.ac.uk/dynamic_topography/), 2016.

Armitage, T. W. K., Bacon, S., Ridout, A. L., Petty, A. A., Wolbach, S., and Tsamados, M.: Arctic Ocean surface geostrophic circulation 2003–2014, *The Cryosphere*, 2017.

935 Armitage, T. W. K., Manucharyan, G. E., Petty, A. A., Kwok, R., and Thompson, A. F.: Enhanced eddy activity in the Beaufort Gyre in response to sea ice loss, *Nature Communications*, 11, 761, <https://doi.org/10.1038/s41467-020-14449-z>, 2020.

Auger, M., Sallée, J., Thompson, A. F., Pauthenet, E., and Prandi, P.: Southern Ocean Ice-Covered Eddy Properties From Satellite Altimetry, *Journal of Geophysical Research: Oceans*, 128, e2022JC019363, <https://doi.org/10.1029/2022JC019363>, 2023.

940 Barnier, B., Blaker, A., Biastoch, A., Boening, C., Coward, A. C., Deshayes, J., Duche, A., Hirschi, J., Sommer, J. L., Madec, G., Maze, G., Molines, J. M., New, A., Penduff, T., Scheinert, M., Talandier, C., and Treguier, A. M.: DRAKKAR:develop ing high resolution ocean components for European Earth system models, 2014.

Barton, B. I., Lique, C., Lenn, Y., and Talandier, C.: An Ice-Ocean Model Study of the Mid-2000s Regime Change in the Barents Sea, *Journal of Geophysical Research: Oceans*, 127, e2021JC018280, <https://doi.org/10.1029/2021JC018280>, 2022.

945 Batrak, Y. and Müller, M.: On the warm bias in atmospheric reanalyses induced by the missing snow over Arctic sea-ice, *Nature Communications*, 10, 4170, <https://doi.org/10.1038/s41467-019-11975-3>, 2019.

Beech, N., Rackow, T., Semmler, T., and Jung, T.: High-latitude Southern Ocean eddy activity projected to evolve with anthropogenic climate change, *Communications Earth & Environment*, 6, <https://doi.org/10.1038/s43247-025-02221-4>, publisher: Springer Science and Business Media LLC, 2025.

950 Carpenter, J. R. and Timmermans, M.: Deep mesoscale eddies in the Canada Basin, Arctic Ocean, *Geophysical Research Letters*, 39, 2012GL053025, <https://doi.org/10.1029/2012GL053025>, 2012.

Cassianides, A., Lique, C., Tréguier, A., Meneghelli, G., and De Marez, C.: Observed Spatio-Temporal Variability of the Eddy-Sea Ice Interactions in the Arctic Basin, *Journal of Geophysical Research: Oceans*, 128, e2022JC019469, <https://doi.org/10.1029/2022JC019469>, 2023.

955 Cavalieri, D. J., Gloersen, P., and Campbell, W. J.: Determination of sea ice parameters with the NIMBUS 7 SMMR, *Journal of Geophysical Research: Atmospheres*, 89, 5355–5369, <https://doi.org/10.1029/JD089iD04p05355>, 1984.

Chelton, D. B., Schlax, M. G., Samelson, R. M., and De Szoeke, R. A.: Global observations of large oceanic eddies, *Geophysical Research Letters*, 34, 2007GL030812, <https://doi.org/10.1029/2007GL030812>, 2007.

Chelton, D. B., Schlax, M. G., and Samelson, R. M.: Global observations of nonlinear mesoscale eddies, *Progress in Oceanography*, 91, 167–216, <https://doi.org/10.1016/j.pocean.2011.01.002>, 2011.

960 Comiso, J. C.: Characteristics of Arctic winter sea ice from satellite multispectral microwave observations, *Journal of Geophysical Research*, 91, 975, <https://doi.org/10.1029/JC091iC01p00975>, 1986.

Corlett, W. B. and Pickart, R. S.: The Chukchi slope current, *Progress in Oceanography*, 153, 50–65, <https://doi.org/10.1016/j.pocean.2017.04.005>, 2017.

D'Asaro, E. A.: Generation of submesoscale vortices: A new mechanism, *Journal of Geophysical Research: Oceans*, 93, 6685–6693, 965 https://doi.org/10.1029/JC093iC06p06685, 1988.

De Lavergne, C., Madec, G., Capet, X., Maze, G., and Roquet, F.: Getting to the bottom of the ocean, *Nature Geoscience*, 9, 857–858, https://doi.org/10.1038/ngeo2850, 2016.

DiGirolamo, N., Parkinson, C., Cavalieri, D., Gloersen, P., and Zwally, H.: Sea Ice Concentrations from Nimbus-7 SMMR and DMSP SSM/I-SSMIS Passive Microwave Data, https://doi.org/10.5067/MPYG15WAA4WX, 2022.

Dupont, F., Higginson, S., Bourdallé-Badie, R., Lu, Y., Roy, F., Smith, G. C., Lemieux, J.-F., Garric, G., and Davidson, F.: A high-resolution ocean and sea-ice modelling system for the Arctic and North Atlantic oceans, *Geoscientific Model Development*, 8, 1577–1594, https://doi.org/10.5194/gmd-8-1577-2015, 2015.

Giles, K. A.: Western Arctic Ocean freshwater storage increased by wind-driven spin-up of the Beaufort Gyre, *NATURE GEOSCIENCE*, 5, 2012.

Giulivi, C. F. and Gordon, A. L.: Isopycnal displacements within the Cape Basin thermocline as revealed by the Hydrographic Data Archive, Deep Sea Research Part I: Oceanographic Research Papers, 53, 1285–1300, https://doi.org/10.1016/j.dsr.2006.05.011, 2006.

Gupta, M., Gürcan, E., and Thompson, A. F.: Eddy-Induced Dispersion of Sea Ice Floes at the Marginal Ice Zone, *Geophysical Research Letters*, 51, e2023GL105 656, https://doi.org/10.1029/2023GL105656, 2024.

Hersbach, H., Bell, B., Berrisford, P., Hirahara, S., Horányi, A., Muñoz-Sabater, J., Nicolas, J., Peubey, C., Radu, R., Schepers, D., Simmons, 980 A., Soci, C., Abdalla, S., Abellan, X., Balsamo, G., Bechtold, P., Biavati, G., Bidlot, J., Bonavita, M., De Chiara, G., Dahlgren, P., Dee, D., Diamantakis, M., Dragani, R., Flemming, J., Forbes, R., Fuentes, M., Geer, A., Haimberger, L., Healy, S., Hogan, R. J., Hólm, E., Janisková, M., Keeley, S., Laloyaux, P., Lopez, P., Lupu, C., Radnoti, G., De Rosnay, P., Rozum, I., Vamborg, F., Villaume, S., and Thépaut, J.: The ERA5 global reanalysis, *Quarterly Journal of the Royal Meteorological Society*, 146, 1999–2049, https://doi.org/10.1002/qj.3803, 2020.

Hu, X., Myers, P. G., and Lu, Y.: Pacific Water Pathway in the Arctic Ocean and Beaufort Gyre in Two Simulations With Different Horizontal Resolutions, *Journal of Geophysical Research*, 2019.

Hunkins, K. L.: Subsurface eddies in the Arctic Ocean\*, Tech. rep., Pergamon Press, volume: 21, 1974.

Isern-Fontanet, J., Garcia-Ladona, E., and Font, J.: Identification of Marine Eddies from Altimetric Maps, *JOURNAL OF ATMOSPHERIC AND OCEANIC TECHNOLOGY*, 20, 2003.

Karcher, M., Smith, J. N., Kauker, F., Gerdes, R., and Smethie, W. M.: Recent changes in Arctic Ocean circulation revealed by iodine-129 observations and modeling, *Journal of Geophysical Research: Oceans*, 117, https://doi.org/10.1029/2011JC007513, publisher: Blackwell Publishing Ltd, 2012.

Kinnard, C., Zdanowicz, C. M., Fisher, D. A., Isaksson, E., de Vernal, A., and Thompson, L. G.: Reconstructed changes in Arctic sea ice over the past 1,450 years, *Nature*, 479, 509–512, https://doi.org/10.1038/nature10581, publisher: Nature Publishing Group, 2011.

Kozlov, I. E., Artamonova, A. V., Manucharyan, G. E., and Kubryakov, A. A.: Eddies in the Western Arctic Ocean From Space-borne SAR Observations Over Open Ocean and Marginal Ice Zones, *Journal of Geophysical Research: Oceans*, 124, 6601–6616, https://doi.org/10.1029/2019JC015113, 2019.

Kubryakov, A. A., Kozlov, I. E., and Manucharyan, G. E.: Large Mesoscale Eddies in the Western Arctic Ocean From Satellite Altimetry Measurements, *Journal of Geophysical Research: Oceans*, 126, e2020JC016 670, https://doi.org/10.1029/2020JC016670, 2021.

Kwok, R.: Arctic sea ice thickness, volume, and multiyear ice coverage: losses and coupled variability (1958–2018), *Environmental Research Letters*, 13, 105 005, https://doi.org/10.1088/1748-9326/aae3ec, 2018.

1005 Lellouche, J.-M., Greiner, E., Le Galloudec, O., Garric, G., Regnier, C., Drevillon, M., Benkiran, M., Testut, C.-E., Bourdalle-Badie, R., Gasparin, F., Hernandez, O., Levier, B., Drillet, Y., Remy, E., and Le Traon, P.-Y.: Recent updates to the Copernicus Marine Service global ocean monitoring and forecasting real-time 112° high-resolution system, *Ocean Science*, 14, 1093–1126, <https://doi.org/10.5194/os-14-1093-2018>, 2018.

Levitus, S., Locarnini, R. A., Boyer, T. P., Mishonov, A. V., Antonov, J. I., Garcia, H. E., Baranova, O. K., Zweng, M. M., Johnson, D. R., and Seidov, D.: World ocean atlas 2009, Volume 1: Temperature, Tech. rep., U.S. Government Printing Office, Washington, D.C, 2010.

Li, J., Pickart, R. S., Lin, P., Bahr, F., Arrigo, K. R., Juranek, L., and Yang, X.: The Atlantic Water Boundary Current in the Chukchi Borderland and Southern Canada Basin, *Journal of Geophysical Research: Oceans*, 125, e2020JC016197, <https://doi.org/10.1029/2020JC016197>, 2020.

1010 Li, X., Wang, Q., Danilov, S., Koldunov, N., Liu, C., Müller, V., Sidorenko, D., and Jung, T.: Eddy activity in the Arctic Ocean projected to surge in a warming world, *Nature Climate Change*, 14, 156–162, <https://doi.org/10.1038/s41558-023-01908-w>, publisher: Nature Publishing Group, 2024.

1015 Lique, C. and Johnson, H. L.: Is there any imprint of the wind variability on the Atlantic Water circulation within the Arctic Basin?, *Geophysical Research Letters*, 2015.

Lique, C., Johnson, H. L., and Davis, P. E. D.: On the Interplay between the Circulation in the Surface and the Intermediate Layers of the Arctic Ocean, *JOURNAL OF PHYSICAL OCEANOGRAPHY*, 45, 2015.

Liu, C., Wang, Q., Danilov, S., Koldunov, N., Müller, V., Li, X., Sidorenko, D., and Zhang, S.: Spatial Scales of Kinetic Energy in the Arctic Ocean, *Journal of Geophysical Research: Oceans*, 129, e2023JC020013, <https://doi.org/10.1029/2023JC020013>, 2024.

1020 Locarnini, R. A., Mishonov, A. V., Baranova, O. K., Reagan, J. R., Boyer, T. P., Seidov, D., Wang, Z., Garcia, H. E., Bouchard, C., Cross, S. L., Paver, C. R., and Dukhovskoy, D.: World Ocean Atlas 2023, Volume 1: Temperature, <https://doi.org/10.25923/54BH-1613>, publisher: NOAA National Centers for Environmental Information, 2024.

MacKinnon, J. A., Simmons, H. L., Hargrove, J., Thomson, J., Peacock, T., Alford, M. H., Barton, B. I., Boury, S., Brenner, S. D., Couto, N., Danielson, S. L., Fine, E. C., Graber, H. C., Guthrie, J., Hopkins, J. E., Jayne, S. R., Jeon, C., Klenz, T., Lee, C. M., Lenn, Y.-D., Lucas, A. J., Lund, B., Mahaffey, C., Norman, L., Rainville, L., Smith, M. M., Thomas, L. N., Torres-Valdés, S., and Wood, K. R.: A warm jet in a cold ocean, *Nature Communications*, 12, 2418, <https://doi.org/10.1038/s41467-021-22505-5>, 2021.

1025 Madec, G., Bell, M., Blaker, A., Bricaud, C., Bruciaferri, D., Castrillo, M., Calvert, D., Jérôme Chanut, Clementi, E., Coward, A., Epicoco, I., Éthé, C., Ganderton, J., Harle, J., Hutchinson, K., Iovino, D., Lea, D., Lovato, T., Martin, M., Martin, N., Mele, F., Martins, D., Masson, S., Mathiot, P., Mocavero, S., Müller, S., Nurser, A. G., Paronuzzi, S., Peltier, M., Person, R., Rousset, C., Rynders, S., Samson, G., Téchené, S., Vancoppenolle, M., and Wilson, C.: NEMO Ocean Engine Reference Manual, <https://doi.org/10.5281/ZENODO.1464816>, publisher: Zenodo Version Number: v4.2.1, 2023.

Manley, T. O. and Hunkins, K.: Mesoscale eddies of the Arctic Ocean, *Journal of Geophysical Research: Oceans*, 90, 4911–4930, <https://doi.org/10.1029/JC090iC03p04911>, 1985.

1030 Manucharyan, G. E. and Isachsen, P. E.: Critical Role of Continental Slopes in Halocline and Eddy Dynamics of the Ekman-Driven Beaufort Gyre, *Journal of Geophysical Research: Oceans*, 124, 2679–2696, <https://doi.org/10.1029/2018JC014624>, publisher: Blackwell Publishing Ltd, 2019.

Manucharyan, G. E. and Spall, M. A.: Wind-driven freshwater buildup and release in the Beaufort Gyre constrained by mesoscale eddies, *Geophysical Research Letters*, 43, 273–282, <https://doi.org/10.1002/2015GL065957>, 2016.

Manucharyan, G. E. and Stewart, A. L.: Stirring of interior potential vorticity gradients as a formation mechanism for large subsurface-  
1040 intensified eddies in the Beaufort Gyre, *Journal of Physical Oceanography*, <https://doi.org/10.1175/jpo-d-21-0040.1>, publisher: American Meteorological Society, 2022.

Manucharyan, G. E. and Thompson, A. F.: Heavy footprints of upper-ocean eddies on weakened Arctic sea ice in marginal ice zones, 2022.

Manucharyan, G. E. and Timmermans, M.-L.: Generation and Separation of Mesoscale Eddies from Surface Ocean Fronts, *Journal of Physical Oceanography*, 43, 2545–2562, <https://doi.org/10.1175/JPO-D-13-094.1>, 2013.

1045 Manucharyan, G. E., Spall, M. A., and Thompson, A. F.: A Theory of the Wind-Driven Beaufort Gyre Variability, *Journal of Physical Oceanography*, 46, 3263–3278, <https://doi.org/10.1175/JPO-D-16-0091.1>, 2016.

Manucharyan, G. E., Lopez-Acosta, R., and Wilhelms, M. M.: Spinning ice floes reveal intensification of mesoscale eddies in the western Arctic Ocean, *Scientific Reports*, 12, 7070, <https://doi.org/10.1038/s41598-022-10712-z>, 2022.

Martin, T., Tsamados, M., Schroeder, D., and Feltham, D. L.: The impact of variable sea ice roughness on changes in Arctic Ocean surface stress: A model study, *Journal of Geophysical Research: Oceans*, 121, 1931–1952, <https://doi.org/10.1002/2015JC011186>, *eprint*: <https://agupubs.onlinelibrary.wiley.com/doi/pdf/10.1002/2015JC011186>, 2016.

1050 Martínez-Moreno, J., Lique, C., and Talandier, C.: Sea Ice Heterogeneity as a Result of Ocean Eddy Activity During the Ice Growth Season, *Geophysical Research Letters*, 52, e2024GL113645, <https://doi.org/10.1029/2024GL113645>, 2025.

McLaughlin, F. A., Carmack, E. C., Williams, W. J., Zimmermann, S., Shimada, K., and Itoh, M.: Joint effects of boundary currents and 1055 thermohaline intrusions on the warming of Atlantic water in the Canada Basin, 1993–2007, *Journal of Geophysical Research: Oceans*, 114, 2008JC005001, <https://doi.org/10.1029/2008JC005001>, 2009.

Meier, W. and Stroeve, J.: An Updated Assessment of the Changing Arctic Sea Ice Cover, *Oceanography*, <https://doi.org/10.5670/oceanog.2022.114>, 2022.

1060 Meneghelli, G., Marshall, J., Campin, J. M., Doddridge, E., and Timmermans, M. L.: The Ice–Ocean Governor: Ice–Ocean Stress Feedback Limits Beaufort Gyre Spin-Up, *Geophysical Research Letters*, 45, 11,293–11,299, <https://doi.org/10.1029/2018GL080171>, publisher: Blackwell Publishing Ltd, 2018a.

Meneghelli, G., Marshall, J., Timmermans, M.-L., and Scott, J.: Observations of Seasonal Upwelling and Downwelling in the Beaufort Sea Mediated by Sea Ice, *JOURNAL OF PHYSICAL OCEANOGRAPHY*, 48, 2018b.

1065 Meneghelli, G., Doddridge, E., Marshall, J., Scott, J., and Campin, J.-M.: Exploring the Role of the “Ice–Ocean Governor” and Mesoscale Eddies in the Equilibration of the Beaufort Gyre: Lessons from Observations, *JOURNAL OF PHYSICAL OCEANOGRAPHY*, 50, 2020.

Meneghelli, G., Marshall, J., Lique, C., Isachsen, L. E., Doddridge, E., Campin, J.-M., Regan, H., and Talandier, C.: Genesis and Decay of Mesoscale Baroclinic Eddies in the Seasonally Ice-Covered Interior Arctic Ocean, *JOURNAL OF PHYSICAL OCEANOGRAPHY*, 51, 2021.

Meredith, M., Heywood, K., Dennis, P., Goldson, L., White, R., Fahrbach, E., Schauer, U., and Østerhus, S.: Freshwater fluxes through the 1070 Western Fram Strait, *Geophysical Research Letters*, 28, 1615–1618, <https://doi.org/10.1029/2000GL011992>, 2001.

Muilwijk, M., Hattermann, T., Martin, T., and Granskog, M. A.: Future sea ice weakening amplifies wind-driven trends in surface stress and Arctic Ocean spin-up, *Nature Communications*, 15, 6889, <https://doi.org/10.1038/s41467-024-50874-0>, 2024.

Nencioli, F., Dong, C., Dickey, T., Washburn, L., and McWilliams, J. C.: A Vector Geometry–Based Eddy Detection Algorithm and Its 1075 Application to a High-Resolution Numerical Model Product and High-Frequency Radar Surface Velocities in the Southern California Bight, *Journal of Atmospheric and Oceanic Technology*, 27, 564–579, <https://doi.org/10.1175/2009JTECHO725.1>, 2010.

Nurser, A. J. G. and Bacon, S.: Arctic Ocean Rossby radius Eddy length scales and the Rossby radius in the Arctic Ocean Arctic Ocean Rossby radius, *Ocean Sci. Discuss*, 10, 1807–1831, <https://doi.org/10.5194/osd-10-1807-2013>, 2013.

Okubo, A.: Horizontal dispersion of floatable particles in the vicinity of velocity singularities such as convergences, *Deep Sea Research and Oceanographic Abstracts*, 17, 445–454, [https://doi.org/10.1016/0011-7471\(70\)90059-8](https://doi.org/10.1016/0011-7471(70)90059-8), 1970.

1080 Pasquero, C., Provenzale, A., and Babiano, A.: Parameterization of dispersion in two-dimensional turbulence, *Journal of Fluid Mechanics*, 439, 279–303, <https://doi.org/10.1017/S0022112001004499>, 2001.

Pedlosky, J.: *Geophysical Fluid Dynamics*, Springer edn., 1982.

Pickart, R. S., Weingartner, T. J., Pratt, L. J., Zimmermann, S., and Torres, D. J.: Flow of winter-transformed Pacific water into the Western Arctic, *Deep Sea Research Part II: Topical Studies in Oceanography*, 52, 3175–3198, <https://doi.org/10.1016/j.dsr2.2005.10.009>, 2005.

1085 Planat, N., Tremblay, L. B., Dufour, C. O., and Straub, D.: Seasonal and Decadal Geostrophic Pathways of Pacific and Atlantic Waters in the Arctic Amerasian Basin From Observations, *Journal of Geophysical Research: Oceans*, 130, e2024JC021560, <https://doi.org/10.1029/2024JC021560>, 2025.

Proshutinsky, A., Krishfield, R., Timmermans, M.-L., Toole, J., Carmack, E., McLaughlin, F., Williams, W. J., Zimmermann, S., Itoh, M., and Shimada, K.: Beaufort Gyre freshwater reservoir: State and variability from observations, 2009.

1090 Rampal, P., Weiss, J., and Marsan, D.: Positive trend in the mean speed and deformation rate of Arctic sea ice, 1979–2007, *Journal of Geophysical Research: Oceans*, 114, <https://doi.org/10.1029/2008JC005066>, \_eprint: <https://agupubs.onlinelibrary.wiley.com/doi/pdf/10.1029/2008JC005066>, 2009.

Reagan, J. R., Seidov, D., Wang, Z., Dukhovskoy, D., Boyer, T. P., Locarnini, R. A., Baranova, O. K., Mishonov, A. V., Garcia, H. E., Bouchard, C., Cross, S. L., and Paver, C. R.: *World Ocean Atlas 2023, Volume 2: Salinity*, <https://doi.org/10.25923/70QT-9574>, publisher: NOAA National Centers for Environmental Information, 2024.

1095 Regan, H. C., Lique, C., and Armitage, T. W. K.: The Beaufort Gyre Extent, Shape, and Location Between 2003 and 2014 From Satellite Observations, *Journal of Geophysical Research*, 2019.

Regan, H. C., Lique, C., Talandier, C., and Meneghelli, G.: Response of Total and Eddy Kinetic Energy to the Recent Spinup of the Beaufort Gyre, *JOURNAL OF PHYSICAL OCEANOGRAPHY*, 50, 2020.

1100 Rieck, J. K., Dufour, C. O., Nadeau, L.-P., and Thompson, A. F.: Heat Transport toward Sea Ice by Transient Processes and Coherent Mesoscale Eddies in an Idealized Southern Ocean, *Journal of Physical Oceanography*, 55, 377–396, <https://doi.org/10.1175/JPO-D-24-0073.1>, 2025a.

Rieck, J. K., Martínez Moreno, J., Lique, C., Dufour, C. O., and Talandier, C.: Mean Kinetic Energy and Its Projected Changes Dominate Over Eddy Kinetic Energy in the Arctic Ocean, *Geophysical Research Letters*, 52, e2025GL117957, <https://doi.org/10.1029/2025GL117957>, 2025b.

1110 Smith, K. S. and Vallis, G. K.: The Scales and Equilibration of Midocean Eddies: Freely Evolving Flow, *Journal of Physical Oceanography*, 31, 554–571, [https://doi.org/10.1175/1520-0485\(2001\)031<0554:TSAEOM>2.0.CO;2](https://doi.org/10.1175/1520-0485(2001)031<0554:TSAEOM>2.0.CO;2), 2001.

Spall, M. A., Pickart, R. S., Fratantoni, P. S., and Plueddemann, A. J.: Western Arctic Shelfbreak Eddies: Formation and Transport, *Journal of Physical Oceanography*, 38, 1644–1668, <https://doi.org/10.1175/2007JPO3829.1>, 2008.

Spall, M. A., Pickart, R. S., Li, M., Itoh, M., Lin, P., Kikuchi, T., and Qi, Y.: Transport of Pacific Water Into the Canada Basin and the Formation of the Chukchi Slope Current, *Journal of Geophysical Research: Oceans*, 123, 7453–7471, <https://doi.org/10.1029/2018JC013825>, publisher: Blackwell Publishing Ltd, 2018.

Stadnyk, T. A., Tefs, A., Broesky, M., Déry, S. J., Myers, P. G., Ridenour, N. A., Koenig, K., Vonderbank, L., and Gustafsson, D.: Changing freshwater contributions to the Arctic, *Elementa: Science of the Anthropocene*, 9, 00 098, <https://doi.org/10.1525/elementa.2020.00098>, 2021.

1115 Stegner, A., Le Vu, B., Dumas, F., Ghannami, M. A., Nicolle, A., Durand, C., and Faugere, Y.: Cyclone-Anticyclone Asymmetry of Eddy Detection on Gridded Altimetry Product in the Mediterranean Sea, *Journal of Geophysical Research: Oceans*, 126, e2021JC017475, <https://doi.org/10.1029/2021JC017475>, 2021.

Talandier, C. and Lique, C.: CREG12.L75-REF12, <https://doi.org/10.5281/ZENODO.13491948>, 2024.

1120 Timmermans, M.-L., Toole, J., Proshutinsky, A., Krishfield, R., and Plueddemann, A.: Eddies in the Canada Basin, Arctic Ocean, Observed from Ice-Tethered Profilers, *Journal of Physical Oceanography*, 38, 133–145, <https://doi.org/10.1175/2007JPO3782.1>, 2008.

Toole, J., Krishfield, R., Timmermans, M.-L., and Proshutinsky, A.: The Ice-Tethered Profiler: Argo of the Arctic, *Oceanography*, 24, 126–135, <https://doi.org/10.5670/oceanog.2011.64>, 2011.

Tulloch, R., Marshall, J., Hill, C., and Smith, K. S.: Scales, Growth Rates, and Spectral Fluxes of Baroclinic Instability in the Ocean, *Journal 1125 of Physical Oceanography*, 41, 1057–1076, <https://doi.org/10.1175/2011JPO4404.1>, 2011.

Vancoppenolle, M., Rousset, C., Blockley, E., Aksenov, Y., Feltham, D., Fichefet, T., Garric, G., Guemas, V., Iovino, D., Keeley, S., Madec, G., Massonnet, F., Ridley, J., Schroeder, D., and Tietsche, S.: SI3, the NEMO Sea Ice Engine, <https://doi.org/10.5281/ZENODO.7534900>, publisher: Zenodo Version Number: 4.2release\_doc1.0, 2023.

von Appen, W.-J., Baumann, T. M., Janout, M. A., Koldunov, N. V., Lenn, Y.-D., Pickart, R. S., and Wang, Q.: Eddies and the Distribution 1130 of Eddy Kinetic Energy in the Arctic Ocean, 35, 42–51, 2022.

Wang, Q., Koldunov, N. V., Danilov, S., Sidorenko, D., Wekerle, C., Scholz, P., Bashmachnikov, I. L., and Jung, T.: Eddy Kinetic Energy in the Arctic Ocean From a Global Simulation With a 1-km Arctic, *Geophysical Research Letters*, 47, <https://doi.org/10.1029/2020GL088550>, publisher: Blackwell Publishing Ltd, 2020.

Watanabe, E.: Beaufort shelf break eddies and shelf-basin exchange of Pacific summer water in the western Arctic Ocean detected by satellite 1135 and modeling analyses, *Journal of Geophysical Research*, 116, C08 034, <https://doi.org/10.1029/2010JC006259>, 2011.

Watanabe, E., Onodera, J., Harada, N., Honda, M. C., Kimoto, K., Kikuchi, T., Nishino, S., Matsuno, K., Yamaguchi, A., Ishida, A., and Kishi, M. J.: Enhanced role of eddies in the Arctic marine biological pump, *Nature Communications*, 5, 3950, <https://doi.org/10.1038/ncomms4950>, 2014.

Weiss, J.: The dynamics of enstrophy transfer in two-dimensional hydrodynamics, *Physica D: Nonlinear Phenomena*, 48, 273–294, 1140 [https://doi.org/10.1016/0167-2789\(91\)90088-Q](https://doi.org/10.1016/0167-2789(91)90088-Q), 1991.

Weiss-Gibbons, T., Tefs, A., Hu, X., Stadnyk, T., and Myers, P. G.: Sensitivity of Simulated Arctic Ocean Salinity and Strait Transport to Interannually Variable Hydrologic Model Based Runoff, *Journal of Geophysical Research: Oceans*, 129, e2023JC020536, <https://doi.org/10.1029/2023JC020536>, 2024.

Woodgate, R. A.: Increases in the Pacific inflow to the Arctic from 1990 to 2015, and insights into seasonal trends and driving mechanisms 1145 from year-round Bering Strait mooring data, *Progress in Oceanography*, 160, 124–154, <https://doi.org/10.1016/j.pocean.2017.12.007>, publisher: Elsevier Ltd, 2018.

Zhang, J. and Rothrock, D. A.: Modeling Global Sea Ice with a Thickness and Enthalpy Distribution Model in Generalized Curvilinear Coordinates, *Monthly Weather Review*, 131, 845–861, [https://doi.org/10.1175/1520-0493\(2003\)131<0845:MGSIWA>2.0.CO;2](https://doi.org/10.1175/1520-0493(2003)131<0845:MGSIWA>2.0.CO;2), 2003.

Zhang, J., Steele, M., Runciman, K., Dewey, S., Morison, J., Lee, C., Rainville, L., Cole, S., Krishfield, R., Timmermans, M.-L., and Toole, 1150 J.: The Beaufort Gyre intensification and stabilization: A model-observation synthesis, *Journal of Geophysical Research*, 2016.

Zhao, M. and Timmermans, M. L.: Vertical scales and dynamics of eddies in the Arctic Ocean's Canada Basin, *Journal of Geophysical Research: Oceans*, 120, 8195–8209, <https://doi.org/10.1002/2015JC011251>, publisher: Blackwell Publishing Ltd, 2015.

Zhao, M., Timmermans, M.-L., Cole, S., Krishfield, R., Proshutinsky, A., and Toole, J.: Characterizing the eddy field in the Arctic Ocean halocline, *Journal of Geophysical Research: Oceans*, 119, 8800–8817, <https://doi.org/10.1002/2014JC010488>, 2014.

1155 Zhao, M., Timmermans, M. L., Cole, S., Krishfield, R., and Toole, J.: Evolution of the eddy field in the Arctic Ocean's Canada Basin, 2005–2015, *Geophysical Research Letters*, 43, 8106–8114, <https://doi.org/10.1002/2016GL069671>, publisher: Blackwell Publishing Ltd, 2016.